

1 Constraint-based modeling identifies metabolic vulnerabilities during the epithelial to
2 mesenchymal transition

3 [Scott Campit](#), Venkateshwar G. Keshamouni*, [Sriram Chandrasekaran](#)*

4

5 *- Corresponding authors

6

7 ¹Program in Chemical Biology, University of Michigan, Ann Arbor, MI, 48109, USA.

8 ²Center for Bioinformatics and Computational Medicine, Ann Arbor, MI, 48109, USA.

9 ³Department of Biomedical Engineering, University of Michigan, Ann Arbor, MI, 48109, USA.

10 ⁴Rogel Cancer Center, University of Michigan Medical School, Ann Arbor, MI, 48109, USA.

11 ⁵Division of Pulmonary and Critical Care Medicine, Department of Internal Medicine, University
12 of Michigan, Ann Arbor, MI 48109

13

14

15

16

17

18

19 Abstract

20 Epithelial-to-mesenchymal transition (EMT) is a developmentally conserved cellular process
21 critical for tumor metastasis. EMT enables malignant epithelial cells to acquire mesenchymal-
22 like migratory and invasive phenotype. During EMT cancer cells undergo extensive metabolic
23 reprogramming that correlates with the suppression of proliferation, and stimulation of the
24 energy-intensive migratory behavior. However, the causal relationship between metabolic
25 changes and coordinated physiological phenotypes that occur during EMT is still unclear. We
26 used bulk time-course transcriptomics and proteomics, and single-cell transcriptomics from five
27 independent EMT studies in A549 lung adenocarcinoma cells to simulate metabolic network
28 activity using constraint-based modeling. Model predictions were validated using literature
29 mining, experimental studies and CRISPR-Cas9 essentiality screens. We uncovered temporal
30 metabolic dependencies in glycolysis and glutamine metabolism reactions, and experimentally
31 validated isoform-specific dependency on Enolase3 for cell survival during EMT. Together, our
32 approach uncovered temporally regulated cell-state-specific metabolic dependencies in cells
33 undergoing EMT.

34

35

36

37 Introduction

38 EMT is a reversible developmental process stimulated by extracellular signals that
39 facilitate the transition from an epithelial (E) cell to a motile and invasive mesenchymal-like (M)
40 cells, enabling circulating tumor cells to initiate metastasis ([Pastushenko and Blanpain 2019](#)).
41 More importantly, EMT is not a binary process but occurs through a spectrum of distinct
42 intermediate states with potential functional consequences. The cytokine - transforming growth
43 factor β (TGF- β), is a potent inducer of EMT. Consistently, TGF- β levels are highly upregulated
44 and directly correlate with tumor progression, enhanced invasion, metastasis, and poor survival
45 in patients with non-small cell lung cancer (NSCLC) ([Padua and Massagué 2009](#)). Cell culture
46 models of TGF- β -induced EMT serves as robust *in vitro* model to investigate mechanisms of
47 metastasis. In addition to metastasis, the process of EMT-MET is implicated in several clinically
48 relevant aspects including, tumor heterogeneity, stemness, and drug resistance ([Ramesh et al.](#)
49 [2020](#)). Understanding underlying regulatory mechanisms is essential to develop therapeutic
50 strategies that can prevent EMT or promote MET to inhibit metastasis.

51 Extensive molecular and structural changes that occur during EMT can potentially induce
52 robust metabolic reprogramming to support changing cellular phenotypes. Cancers show
53 enhanced glycolytic pathway activity even in the presence of oxygen, via the Warburg effect
54 ([Vander Heiden et al. 2009](#)). It is now clear that the Warburg effect is not restricted to cancer cells
55 but it is an adaptive physiological program that occurs in many normal cell types, when cells need
56 rapid ATP production, biomass synthesis and balancing of reactive oxygen species ([Pålsson-](#)
57 [McDermott and O'Neill 2020](#))([Kim et al. 2016](#)), Studies have demonstrated an enhanced
58 glycolytic activity during EMT. However, similar to EMT, metabolic reprogramming may also
59 involve a spectrum of pathway combinations at a given cellular steady state. While several
60 metabolic rewiring strategies have been observed in diverse cancers, a comprehensive systems-
61 level characterization of metabolic reprogramming during the EMT has not been carried out.
62 Methods that can infer metabolic dysregulation using omics data will be invaluable for

63 understanding causal relationship between EMT and metabolic reprogramming.

64 Constraint-Based Optimization and Reconstruction Analysis (COBRA) is a widely used
65 approach for simulating genome-scale metabolic fluxes using omics data. COBRA simulates
66 metabolic fluxes by using the metabolic network architecture, nutrient availability, and omics data
67 as constraints in an optimization problem representing a cellular objective, such as maximizing
68 biomass production ([Orth et al. 2010](#)). COBRA models have inferred metabolic rewiring strategies
69 in several cancer subtypes ([Oruganty et al. 2020](#); [Yizhak et al. 2014](#); [Nilsson et al. 2020](#)). For
70 instance, incorporating metabolomics data to identify synthetically lethal metabolic genes in
71 pancreatic cancer ([Nelson et al. 2020](#)). However, to our knowledge, no one has applied COBRA
72 to study metabolic network heterogeneity during the EMT and characterized the metabolic
73 properties of intermediate states during EMT.

74 We used COBRA to simulate metabolic activity and vulnerabilities during EMT using diverse
75 omics sources, including time-course transcriptomics, proteomics, and single-cell transcriptomics
76 data. Notably, this study applies constraint-based modeling to single-cell cancer transcriptomics
77 data to capture the metabolic heterogeneity during EMT. From our analysis, we were able to
78 identify known metabolic dependencies during EMT, such as uptake of glucose and glutamine.
79 We also predicted new metabolic dependencies including the enolase and GOT1 reactions and
80 those related to alpha-ketoglutarate metabolism. Surprisingly, many of these dependencies were
81 time-specific, suggesting that there is a narrow temporal window during which the cells can be
82 targeted with drugs that inhibit these pathways. We also found metabolic changes that showed
83 consistent trends based on model predictions derived from both the bulk and single-cell studies.
84 Together, our analysis provide a framework to integrate multiple omics datasets to examine tumor
85 metabolic heterogeneity and infer new drug targets.

86 Methods

87 Differential Expression (Bulk Studies)

88 We analyzed two transcriptomics ([Hecker et al. 2009](#); [Keshamouni et al. 2009](#)) and two
89 proteomics ([Keshamouni et al. 2006](#); [Lu et al. 2019](#)) EMT time-course studies with A549 as the
90 cell model undergoing TGF- β induction. All studies compared later time point after TGF- β
91 induction over day 0 to obtain differentially expressed genes and proteins. When possible,
92 authors' methods and provided datasets were used to obtain a list of up- and downregulated
93 gene sets. If no preprocessed data was provided (as in the case of GSE17518), *limma-voom*
94 ([Law et al. 2014](#)) was performed to determine differentially expressed genes between
95 conditions. Additionally, a GAM-LOESS model was used to determine differentially expressed
96 genes in GSE147405 ([Cook and Vanderhyden 2020](#)), aggregating single-cells at the time-
97 course level. The regression coefficients from the GAM-LOESS model were used to determine
98 the sign of regulation (up/down). P-values from *limma-voom* and a GAM-LOESS model were
99 adjusted using the Benjamini-Hochberg method and the significance threshold used was P-
100 value < 0.05. The expression matrix containing statistically significant normalized scores for all
101 metabolic genes across all 5 experiments can be found in **Supplementary Table 1**.

102 103 Individual Cell Differential Expression

104 We computed differentially expressed genes for individual cells without TGF- β removal
105 in GSE147405 to simulate individual cell fluxes and reaction knockout growth rates. Data
106 preprocessing included data scaling, removing contaminant artifacts such as mitochondrial
107 genes, and removing cells with low total gene counts. This was performed on the raw data
108 object. Further, we used the data imputation algorithm MAGIC (Van Dijk, D. et al., 2018) to fill in
109 drop out values. The MAGIC-imputed data was transformed to a Z-score using a Z-score
110 method that subtracts out the median and centers the data based on the median absolute
111 deviation (MAD). The formula for the robust Z-score for a specific gene i in a given cell j is
112 shown in **Equation 1**:

113
$$Z_{i,j} = \frac{x_{i,j} - \text{median}(x_i)}{1.486 \times MAD} [1]$$

114
115 Where 1.486 is a scaling constant. For any given cell, a gene was determined to be
116 upregulated/downregulated if the robust Z-score was positive/negative and the P-value < 0.05.

117
118 **Prioritizing metabolic gene targets across multiple studies**

119 We evaluated the robustness metabolic gene dysregulation across five EMT studies
120 using the following prioritization score η . The method to compute η shown in **Equation 2**:

121
$$\eta_i = M \sum_{i=1}^N \text{abs}(E_i), [2]$$

122
123
124 Where M is the number of studies where the gene was determined to be significant and E_i is the
125 gene effect size (\log_2 fold change or Z-score) for gene i . The prioritization scores were ranked in
126 descending order and used to prioritize reactions for further investigation.

127
128 **COntstraint-Based Reconstruction and Analysis (COBRA)**

129 Flux balance analysis (FBA; [Orth et al. 2010](#)) was used to simulate metabolic activity
130 using the human metabolic reconstruction RECON1 ([Duarte et al. 2007](#)). Cells were assumed to
131 maximize biomass production as the objective function. Differentially expressed metabolic
132 genes that intersected with RECON1 were used as biological constraints to maximize
133 (upregulation) or minimize (downregulation) metabolic flux using a modified form of the iMAT
134 algorithm ([Zur et al. 2010](#); [Shen et al 2019](#)). Parsimonious enzyme usage ([Lewis et al. 2010](#))
135 was an additional assumption to obtain a unique metabolic flux distribution and to minimize
136 fluxes that did not contribute to biomass formation. Metabolic fluxes and growth rates from
137 single gene and reaction knockout simulations were obtained using COBRA. To ensure a
138 feasible growth rate was calculated, we removed genes/reactions that were upregulated in the
139 knockout and set the percent knockout to be 99% to promote a feasible flux solution.

140

141 Differential Metabolic Activity and Knockout Sensitivity Analysis

142 To determine differentially active metabolic reactions, we used the priority score
143 described in equation 1 on the absolute value of the metabolic fluxes. Most reactions show zero
144 flux, and so reactions that showed metabolic activity were considered to be overactive metabolic
145 reactions.

146 To determine the impact metabolic genes have on the growth rate during different
147 stages of EMT, we computed a sensitivity score θ comparing EMT versus control growth rates
148 for each gene knockout. The equation to compute the bulk sensitivity score is shown in

149 Equation 3:

$$150 \theta_r = \text{mean}\left(\frac{\text{cancer}_{i,j} / \text{mean}(\text{cancer}_j)}{\text{control}_{i,j} / \text{mean}(\text{control}_j)}\right) - 1 [3]$$

152 The flux or growth rate was mean-normalized for the control (day 0) and the TGF- β
153 treatment (all other days). Then, the final score was taken as the ratio of the TGF- β treated
154 growth rate over the average control growth rate for a given reaction knockout. The average
155 ratio across all cells was taken as the score to identify differentially sensitive metabolic
156 reactions. The score was centered at 0. The intuition behind θ is as follows: if the score is 0, the
157 gene/reaction knockout has no difference between cancer and control. If the score is less than
158 0, the knockout impacts the cancer cell more than control, and is considered to be essential for
159 cellular growth. To rank and prioritize metabolic targets for experimental validation, we used the
160 same prioritization score as we did to rank differentially expressed genes.
161

162

163 Classifying cancer cell line states

164 Cancer cell lines from the Cancer Cell Line Encyclopedia (CCLE) were annotated by
165 their source from a primary tumor or metastatic tumor. To also classify whether a cell was in the
166 epithelial versus mesenchymal state, we calculated the Z-score and p-value for all genes in the
167 CCLE and mapped them to known EMT markers. Upregulated genes were classified as having

168 a positive Z-score and a significance threshold of p-value < 0.05, while downregulated genes
169 were classified as having a negative Z-score with the same significance threshold.

170 EMT markers (with up- and downregulated signatures) were taken from MSigDB
171 ([Liberzon et al. 2015](#)) across three studies from different tissues of origin induced using TGF- β .
172 We further filtered this list with NSCLC markers without up/downregulation annotations from
173 EMTome ([Vasaikar et al. 2021](#)). The final number of markers obtained for EMT was 14 genes,
174 which were used to classify cancer cell lines (CCLs). We chose to classify cell lines using upper
175 and lower quantiles of gene makers. Up- and downregulated genes from NSCLC CCLs were
176 cross referenced to the list of EMT signatures and labeled as E if the number of signatures was
177 less than 5 genes or M if the number of signatures was greater than 8.

178

179 CRISPR-Cas9 Analysis

180 We analyzed batch corrected CERES Scores ([Pacini et al. 2021](#)) for metabolic genes
181 that were predicted by COBRA to have increased metabolic activity or resulted in a reduction of
182 growth rate from knockout. CERES Scores were separated based on their association with
183 metastatic (Met) and primary (Prim) cell lines, which was determined based on the CCLE
184 metadata ([Barretina et al. 2012](#)). We also compared the CCLE annotations against our own
185 Epithelial (Epi) and Mesenchymal (Mes) annotations, methods described above.

186 To evaluate how well our model predictions related to CERES Scores, we calculated the
187 Pearson correlation coefficient between our predicted growth scores and ratios of Mes / Epi or
188 Met / Prim CERES Scores. Further, we compared the growth scores against different subsets of
189 the CERES Score data, including NSCLC only cell lines and all cell lines.

190

191 Identifying metabolic enzymes and EMT studies for systematic literature 192 validation

193 To be considered for our systematic literature validation, we pooled a list of metabolic
194 enzymes predicted from COBRA from bulk and single-cell reaction knockouts that had lethal

195 reactions in at least 2 studies (growth score < 0). The query was performed using PubMed and
196 Google with the following keywords using AND filtering: “EMT”, “Metabolism”, “A549”,
197 “metastasis”, “cancer”, “cancer metabolism”, and the individual gene of interest. The list of the
198 manually curated results can be found in **Supplementary Table 5**.

199 We expanded the scope of our literature search to encompass all cancer cell lines. The
200 query was manually curated to either support or refute the COBRA predictions. None of the
201 model predictions contradicted the literature. Reaction predictions and their confidence were
202 scored (1-3), where 1 has no evidence based on literature and 3 has strong A549 or lung
203 adenocarcinoma specific evidence. The rules to assign each score for each reaction prediction
204 are shown below:

- 205 • **1:** Prediction has no literature support.
- 206 • **2:** Prediction has literature evidence with general cancer lineages.
- 207 • **3:** Prediction has literature evidence either with specific experiments from A549
208 or related lung adenocarcinoma tissue/cell lines.

209

210 Cell culture, siRNA transfection and EMT induction

211 A549 human lung adenocarcinoma cell line was obtained from the American Type
212 Culture Collection (Manassas, VA) and maintained in RPMI-1640 medium with glutamine
213 supplemented with 10% FBS, penicillin, and streptomycin at 37°C in 5% CO₂. For inducing
214 EMT cells at 40-50% confluency in complete medium were serum starved for 24 hrs and treated
215 with TGF- β (5 ng/ml) for 72 hrs.

216 Isoform specific siRNA for enolases includes a pool of 4 SMART selection-
217 designed synthetic duplexes (Dharmacon's SMARTpool). A scrambled sequence from the
218 same company is used as a control. Cells at 40-50% confluency were transfected with siRNA
219 using Lipofectamine 2000 (Cat No: 18324-012, Invitrogen) and optiMEM medium (Cat No:
220 31985, Gibco) following the manufacturer's instructions. After 6 hours of transfection cells were

221 washed and allowed to recover from transfection in RPMI 1640 medium with 10% FBS before
222 inducing EMT as described above.

223 Apoptosis assays

224 Apoptosis was assessed by two independent methods; 1) *AnnexinV/7-AAD staining (Kit*
225 *from Biolegend Cat# 640922)*: At the end of the EMT experiment described above, all cells
226 (including floating cells) were collected, washed and resuspended in Annexin V binding buffer.
227 100 ul of cell suspension was stained with 5 ul of FITC-Annexin V, followed by 5 ul of 7-AAD
228 staining solution. After 30 min incubation at room temperature in dark, 400 ul of Annexin V
229 binding buffer is added and assessed for Annexin V and 7-AAD staining by flow cytometry. Both
230 Annexin V positive (early apoptotic) and Annexin V and 7-AAD double positive cells (late
231 apoptotic) are added together for assessing total apoptosis. 2) *Assessing Caspase 3 activation*:
232 To assess casapase3 activation during EMT, an artificial caspase3 substrate coupled to a green
233 fluorescent DNA-binding dye (DEVD-Nucview) is added to the cell culture. When caspase3 is
234 activated, it cleaves the DNA-binding dye which enters the nuclei and labels an apoptotic cell
235 with green fluorescence allowing its imaging. Green fluorescent apoptotic cells were imaged
236 under a fluorescent microscope 48 hrs after TGF- β -induced EMT.

237 Results

238 COBRA reveals that cells undergoing EMT exhibit enhanced glycolysis 239 during early and late stages

240 We performed a meta-analysis of differentially expressed genes and proteins across four
241 bulk EMT datasets. Two were RNASeq-based datasets (GSE17708 and GSE17518), and two
242 were proteomics-based datasets (Garcia and Keshamouni). To aggregate the results from
243 multiple studies, we designed a prioritization score to rank the reactions based on effect size
244 and whether or not the gene was significantly expressed in a given study (**Supplementary**
245 **Table 1; Methods**).

246 We simulated the metabolic fluxes for each time-point using the transcriptomics and
247 proteomics data to see how metabolic activity changes over time during EMT using Flux
248 Balance Analysis (FBA; **see Methods**). FBA uses a linear optimization procedure with biological
249 constraints, such as knowledge of the metabolic network structure (known as a stoichiometric
250 (S) matrix) and expression levels as inputs to generate cell-state specific metabolic flux profiles
251 ([O'Brien et al. 2015](#)). FBA assumes that the cell is maximizing an objective, usually its biomass
252 production. While standard FBA outputs multiple flux profiles due to the rank deficiency of the S
253 matrix ([Orth et al. 2010](#)), Parsimonious FBA or pFBA provides a unique flux distribution by
254 assuming optimal enzyme efficiency by minimizing the overall metabolic flux throughout the
255 metabolic network while maximizing biomass production ([Lewis et al. 2010](#)). pFBA identifies the
256 smallest set of active reactions that best support biomass production.

257 Our predictions using pFBA reveal that there are more active reactions during the early
258 and late phases of EMT. During the intermediate phases of EMT, metabolic activity goes down.
259 As cells undergo dramatic structural rearrangements when transitioning to a mesenchymal cell,
260 cells require energetic substrates such as ATP to facilitate these processes. Our metabolic
261 model assumed that these cancer cells were optimizing for increased biomass production, and
262 the reduction of fluxes for biomass production during the intermediate EMT stages suggests that

263 metabolic activity is being siphoned towards other processes such as motility. Our metabolic
264 flux profile data suggests that cancer cells upregulate metabolism initially to build up metabolic
265 substrate levels, and then divert all transcriptional resources towards other processes.

266 Samples within these time-points tend to have similar metabolic functions, as most
267 active reactions are found within central carbon metabolism (glycolysis/gluconeogenesis,
268 pentose phosphate pathway, folate metabolism) and nutrient exchange subsystems. These
269 metabolic pathways contribute to biomass formation. We visualized the top 50 reactions sorted
270 by prioritization scores (**Methods; S. Figure 1; Supplementary Table 2**). The prioritization
271 score takes into consideration the number of studies where a given metabolic gene(s) encoding
272 a reaction was determined to be significant and absolute value of the gene effect size (\log_2 fold
273 change or Z-score). Developing a prioritization score enabled us to filter through 3744 reactions
274 to provide a concise reaction list for downstream analyses.

275
276 Several glycolytic reactions were predicted to have increased metabolic activity and
277 priority scores (**Figure 1A**), which was expected given how cancer cells rewire glycolytic
278 activity, as evidenced by the Warburg effect ([Vander Heiden et al. 2009](#)). Several glycolytic
279 substrates play a role in both cellular survival and cancer proliferation. It has been well
280 established that TGF- β increases expression of several glycolytic enzymes ([Jia et al. 2021](#)). We
281 found that hexokinase, glyceraldehyde-3-phosphate dehydrogenase (GAPDH), and enolase
282 were the top 3 glycolytic reactions that were highly active in both early and late EMT stages,
283 supporting previous studies that suggest glycolysis is directly impacted by TGF- β induction. The
284 timing of metabolic activity suggests that glycolysis is essential for initiating EMT and
285 establishing metastasis at later stages.

286 Genome-scale reaction knockout simulation identifies extensive 287 vulnerabilities in mesenchymal state

288 While our previous analysis focused on reaction fluxes, next we used FBA to simulate
289 the impact of reaction knockout on cellular growth in each time-points across five independent

290 A549 TGF- β induced EMT studies (**S. Figure 2; Supplementary Table 3**). Briefly, each
291 metabolic reaction encoded in the reconstruction was systematically shut off (upper and lower
292 bounds were set to 0) to simulate a “knockout”, while the growth rate objective was optimized.
293 This method allows us to infer the impact systematic reaction knockouts have on cellular
294 growth. We analyzed the distribution of knockouts across bulk experiments and by time-course.
295 The later stage of EMT were predicted to have more vulnerabilities (932 reactions) than in the
296 early stage (874 reactions) and intermediate stage (660 reactions), suggesting mesenchymal
297 cells are more vulnerable to metabolic perturbation (**Figure 2; inset**).

298 We identified over 40 reactions that were specifically sensitive in specific EMT stages
299 and studies (**Figure 2**). These also highlight the technical and biological variance that is
300 observed in EMT studies across different omics modes. Notably, alpha-ketoglutarate (AKG)
301 transport between the cytosol was unique to the intermediate stage in two out of five
302 independent studies. From a mechanistic standpoint, AKG likely suppresses metastasis by
303 counteracting the effects of other oncometabolites such as 2-hydroxyglutarate, succinate, and
304 fumarate ([Wei et al. 2020](#)). While the impact of AKG and cellular differentiation / proliferation
305 has been observed through several nutrient perturbation studies in cancer and stem-cells
306 ([Campit et al., 2021](#)), the exact source and subcellular contribution of AKG and its impact on
307 metastasis is difficult to determine experimentally. Our computational model suggests that
308 knockout of AKG transport between the cytosol and mitochondria has a negative impact during
309 EMT, providing clues about cellular compartment dynamics and their impact on cancer
310 metastasis. We hypothesize that accumulation of AKG within the mitochondria counteracts
311 oncometabolite effects through additional regulatory mechanisms.

312 Two other reactions in central carbon metabolism had high priority scores, namely,
313 enolase (ENO) and lactate dehydrogenase (LDH_L), both predicted from the same EMT
314 proteomics data ([Keshamouni et al. 2006](#)). Upregulated enolase levels are associated with
315 promoting cell growth, migration, and invasion during EMT in various cancers ([Song et al. 2014](#);

316 [Zhao et al. 2015](#)). Further, LDH is highly associated with cancer metastasis, and has been
317 shown to activate EMT in several cancers, including lung cancer, during metastasis ([Hou et al.](#)
318 [2019](#); [Zhang et al. 2018](#)). While it is known that ENO and LDH upregulation and/or increased
319 activity are associated with poor patient prognosis, little is known about how changes in
320 metabolic activity over time leads to differential sensitivity in cancer. Our modeling approach
321 shows that enolase and lactate dehydrogenase are essential during later stages of EMT
322 compared to earlier stages, revealing information about time-dependent sensitivity of these well-
323 known targets for the first time.

324 In addition to nutrient exchange reactions, we found three metabolic reactions that
325 consistently decreased growth upon KO across all time points. Two metabolic enzymes were
326 involved in fatty acid metabolism: Fatty acid CoA ligase hexadecanoate and beta-ketoacyl
327 synthetase. Fatty acid synthase (FASN) is a potential therapeutic target for NSCLC, and beta-
328 ketoacyl synthetase is one component of FASN. Preclinical studies show that beta-ketoacyl
329 synthase inhibition induces apoptosis and stops proliferation in cancer cells *in vitro* and *in vivo*
330 ([Menendez et al. 2004](#); [Pizer et al. 1996](#)).

331 Further, our model suggests two additional reactions that do not have literature backing
332 to be potential therapeutic targets, but are associated with metabolic pathways that are
333 frequently dysregulated across different cancers. Lipid metabolites concentrations have
334 prognostic value, and dysregulated fatty acid metabolism is associated with poor cancer patient
335 prognosis. While it is known that metabolic enzymes such as Fatty Acid CoA Ligases modify
336 ratios of these fatty acids, and that there is differential regulation and expression of these
337 metabolic enzymes in cancer, little is known about the balance of fatty acids and fatty acyl-CoAs
338 and its impact on cancer. Our model suggests that the fatty acid CoA ligase that specifically
339 modifies hexadecanoate contributes highly to EMT and suggests an interesting hypothesis that
340 needs to be validated experimentally, but has high potential as a new avenue for therapeutic
341 intervention.

342 Additionally, we analyzed reactions that either had very strong effects on a single study
343 or were predicted to impact biomass in specific time points in at least two out of five studies (**S.**
344 **Figure 2**). This provided us information about reactions that show temporal-specificity or
345 robustness across datasets. Glucose and aspartate exchange reactions were predicted to be
346 sensitive across all time points and experiments, suggesting that cells in all stages of EMT are
347 sensitive to perturbations to these nutrients. It is well documented in the literature that high
348 glucose levels facilitate migration and invasion processes in EMT for several types of cancer
349 ([Xu et al. 2019](#); [Liu et al. 2016](#)). Additionally, aspartate is crucial to cell proliferation and survival
350 in cancer ([Birsoy et al. 2015](#); [Alkan et al. 2018](#); [Sullivan et al. 2015](#)). Our model also captured
351 aspects of metabolic heterogeneity associated with glutamine metabolism in EMT. We found
352 that cells were dependent on glutamine exchange in early (1 hr) and late (48-72 hrs) time
353 points, while becoming insensitive to glutamine exchange during intermediate stages (8 - 24
354 hrs) (**S. Figure 2; top row**). Glutamine metabolism is essential for sustaining proliferation in
355 many tumor lineages including NSCLC, and the dysregulation of glutaminolysis is a hallmark of
356 cancer metabolism ([Yang et al. 2017](#)). Glutamine regulates the activation of STAT3, a critical
357 transcription factor associated with tumor growth and metastasis ([Cacace et al. 2017](#); [Yang et](#)
358 [al. 2014](#)). Together, these results suggest that our COBRA models can accurately predict well-
359 known impact of nutrient perturbations in cancer and EMT.

360 Isoform-specific role of Enolase 3 in regulating cell survival during EMT

361 Reactions in glycolysis, especially enolase, was identified by both our flux and gene
362 knockout analysis to have high metabolic activity and sensitivity to knockout. During tumor
363 progression, cancer cells must increase glucose metabolism. Owing to the hypoxic tumor
364 microenvironments, cancer cells upregulate glycolytic enzymes, including Enolase (Eno), to
365 support anaerobic proliferation (Warburg effect). Enolase (Eno) is a key glycolytic enzyme that
366 catalyzes the dehydration of 2-phosphoglycerate to phosphoenolpyruvate. It occurs as 3

367 isoforms, Eno1 (ubiquitously expressed in all cells), Eno2 (neuronal specific) and Eno3 (muscle
368 specific) (Chang et al., 2006). Our transcriptomic analysis show that Eno3 the muscle specific
369 isoform which is catalytically more efficient, is 10 fold differentially expressed in cells undergoing
370 EMT (**S. Figure 3**) (Keshamouni et al., 2006). siRNA mediated inhibition of Eno3 selectively
371 induced apoptosis in cells undergoing EMT whereas, inhibition of the ubiquitously expressed
372 isoform, Eno1, did not, as assessed by Annexin-V/PI staining by flow cytometry (**Figure 3A**) and
373 Caspase8 activation assay (**Figure 3B**). These observations suggest that EMT induces
374 reprogramming of glycolysis to an Eno3 dependent pathway to meet the energy demands of
375 migratory and invasive cells. Inhibition of Eno3 will selectively kill cells undergoing EMT and
376 may prevent metastasis.

377 Single-cell knockout simulations reveal metabolic heterogeneity in a cell 378 population undergoing EMT

379 To determine whether the variations observed in bulk dataset analysis are true reflection
380 of metabolic phenotypes at the single cell level, we next analyzed single cell transcriptomics
381 data of A549 cells induced with TGF- β (GSE147405; [Cook & Vanderhyden, 2020](#)). To capture
382 subtle metabolic differences as cells' transition from E to M states, we reconstructed separate
383 models for each cell based on its transcriptomic profile measured in the dataset. To ensure we
384 were observing the transition between E to M in this dataset, we visualized VIM and CDH1
385 expression levels in the UMAP embedding and found that the expression profiles are consistent
386 with what is observed in the literature (**Supplementary Figure 4**). We used the resulting models
387 for 644 individual cells across all time points and computed growth rates after genome-scale
388 reaction knockouts in each individual cell. For comparison with the bulk datasets, we
389 aggregated the cells, taking the average knockout scores across each time point (**Figure 4; S.**
390 **Table 4**). We found that many reactions predicted to impact growth in the single-cell analysis
391 were also sensitive in the bulk analysis (**Table 1, S. Table 5; N = 95 intersected reactions**).

392 To examine how reaction knockout sensitivity changes over EMT progression for the top 5
393 variable central carbon metabolism reactions, we plotted the growth scores for representative
394 reactions that had high variance onto the UMAP embedding (**Figure 5 A-F**). Reactions that
395 were predicted from our bulk knockout profiles including AKG-malate transport, Enolase,
396 Carnitine O-acetyltransferase, and ATP-Citrate Lyase show heterogeneous sensitivity across all
397 time points. Citrate Synthase was predicted to be sensitive across all time points, suggesting
398 that this reaction is critical in all stages of EMT. We also observed metabolic heterogeneity in
399 glutamine metabolism. We found that there was a positive correlation between the master
400 regulator STAT3, glutamine synthetase, and glutamine transporter levels in the single cell data
401 (**S. Figure 5A & B**). This is consistent with studies that have observed that glutamine regulates
402 the activation of STAT3. Overall, our model identifies individual cells that are sensitive to
403 specific reaction knockouts, providing a granular metabolic dependency profile of a population
404 of cells undergoing EMT.

405 406 **Prioritization of metabolic targets during EMT using both bulk and single-** 407 **cell simulations**

408
409 We performed extensive literature curation for genes that were found to show growth
410 reduction upon knockout in both the bulk and single-cell analysis (**Table 1, S. Table 5**; N = 95
411 intersected reactions). These reactions were prioritized based on the number of studies found
412 for each gene query and its relevance to cancer and EMT. Two high confidence predictions that
413 were found in both analyses included Pyruvate Carboxylase and Fructose-Bisphosphate
414 Aldolase, which were shown to contribute specifically to NSCLC progression and metastasis
415 ([Sellers et al. 2015](#); [Fu et al. 2020](#)). Eight reaction predictions had some evidence of being
416 dysregulated in another cancer subtype, but not NSCLC. The remaining 10 reactions have not
417 been highlighted in the literature, and present opportunities for experimental validation.

418 To further assess our model predictions against experimental data, we compared our
419 bulk and single-cell knockout results against batch-corrected CRISPR-Cas9 essentiality
420 knockout screens integrated from the Broad and Sanger Institute ([Pacini et al. 2021](#)). Given the
421 limited availability of CRISPR-Cas9 screenings in EMT studies, we took NSCLC cancer cell
422 lines from the DepMap dataset, which annotated them to be derived either from a primary tumor
423 or a metastatic site. Further, we took EMT signatures from MSigDB and EMTome to classify
424 cancer cell lines from the cancer cell line encyclopedia (CCLE) into epithelial-like or
425 mesenchymal-like cell-lines (**Methods**). When comparing the classification of CCLE cancer
426 annotation with our EMT classification, we found that there was high agreement between cancer
427 cell lines obtained from a primary site and the epithelial state while there was low agreement
428 between the mesenchymal cell state and cell lines from a metastatic site (**Figure 6A**).

429 The essentiality of metabolic enzymes identified from our model predictions were
430 interpreted using the CRISPR gene knockout (CERES) Scores, where a lower score is
431 associated with a higher likelihood that a given gene is essential for survival in a given cell line
432 ([Meyers et al, 2017](#)). A score of 0 was used as the threshold to indicate the median effect of
433 non-sensitive genes. We overlaid the CERES Scores for metabolic genes corresponding to
434 reactions predicted from our sensitivity analysis with the CCLE cancer cell line annotation and
435 our EMT annotation (**Figure 6B and C**). Overall, we found that the median values for both
436 classification methods agreed with each other for the most part. The alpha-ketoglutarate /
437 malate transporter SLC25A11, ENO1, ENO2, ENO3, IDH1, and LDH show lower median
438 CERES scores than the threshold of 0, supporting our model's findings. From this analysis, we
439 were able to identify isoform-specific sensitivity in NSCLC, analogous to our validation of Eno3
440 dependency (**Figure 3**). IDH1 gene depletion is associated with NSCLC essentiality, compared
441 to IDH2 and IDH3 depletion, suggesting that targeting IDH1 expression in NSCLC may be an
442 effective therapy to supplement existing therapeutics that target specific IDH1/2 mutations.

443 To evaluate how well our knockout growth score predictions performed against CRISPR-
444 Cas9 experimental data, we took the ratio of the CERES scores for the Primary site derived
445 NSCLC cell lines to the scores for the Metastatic site derived cell lines for each metabolic gene.
446 We found that the average growth scores and metabolic fluxes agreed significantly with the ratio
447 data with $R = 0.31$ and 0.20 respectively, P -value = 0.005 and 0.036 (**S. Table 6 & 7**). We
448 determined the correlation between our predictions against all cell lines as well, but found that
449 the correlations were not significant with the pan-cancer CERES Score data. These results
450 match our expectations, as our COBRA models were constrained using A549 transcriptomics
451 and proteomics data. We evaluated the quality of each dataset on COBRA predictions, and
452 found that the single-cell RNASeq data best matched the CERES Score ratios (KO $R = 0.27$,
453 KO P -value = 0.01 ; Flux $R = 0.20$, Flux P -value = 0.03 ; **S. Table 6 & 7**) while bulk
454 transcriptomics and proteomics data were weakly correlated ($R < 0.1$; P -value > 0.05 ; all bulk
455 experiments).

456 There are several confounding variables that could contribute to the reduced correlation
457 between our predictions and the experimental data. First, we assumed that cells derived from
458 primary tumor sites have similar metabolic attributes to epithelial-like cells, while metastatic cell
459 lines were similar to mesenchymal cells. We addressed this assumption by re-classifying cells
460 based on EMT gene markers. We obtained similar correlations and p -values from grouping cell
461 lines either using the CCLE annotation or our EMT classification method (**S. Table 8 & 9**).
462 While the transcriptomics and proteomics EMT datasets to build the metabolic models were
463 induced using TGF- β , the cancer cell lines used in the CRISPR screen were not induced with
464 an EMT inducer. Thus, the cell dynamics that occur during EMT are not captured in CRISPR
465 screening data. Finally, we used NSCLC CCLs to evaluate the statistical significance of our
466 results, while our simulations were performed on A549 exclusively. Due to these confounding
467 factors, in contrast to our siRNA knockdown experiment, we found that the CERES scores did
468 not distinguish between the three isoforms of enolase. Despite these assumptions and

469 considerations, we found that our simulations were correlated significantly with the CERES
470 Scores, suggesting that our model is able to extract relevant biological insights.

471 Discussion

472 Here we utilize constraint-based modeling informed by multiple omics data sources to
473 predict metabolic activity and knockout sensitivity during EMT. Our predictions are supported
474 from literature validation, siRNA knockout studies, and CRISPR-Cas9 essentiality panels. We
475 further provide a list of high confidence metabolic reaction dependencies during EMT for future
476 experimental validation. Our approach also provides insights into metabolic activity at the single-
477 cell level, which is not possible to infer with current experimental methodologies.

478 Our modeling identified metabolic enzymes that are novel as well as those with
479 experimental evidence in literature supporting their role in tumor progression. We identified
480 known metabolic reactions that contribute to cancer progression, such as glucose and
481 glutamine transport. We further identified metabolic reactions associated with fatty acid
482 metabolism that contribute to metastasis. We found that most glycolytic reactions were
483 overactive in the early and late stages of EMT. This time-dependent aspect of glycolytic activity
484 was intriguing and suggests a potential vulnerability during EMT. We further experimentally
485 validate the essential role of the enolase reaction in EMT. The enolase enzyme is implicated in
486 cancer progression for various tissue lineages, but so far has not been identified as a crucial
487 player in NSCLC metastasis. Our COBRA modeling approach identified reaction catalyzed by
488 Enolase as highly active during the early and late stages of EMT and predicted enolase
489 knockout to have a negative impact on cellular growth. Enolase has three isoforms with a
490 degree of cell type specific expression. Eno1 is ubiquitously expressed in all cells, Eno2 is
491 neuronal specific and Eno3 is a muscle specific isoform. In our transcriptomic data sets, we
492 observed expression of Eno1 and Eno3, but not Eno2. Even though COBRA analysis did not
493 distinguish between isoforms, we were able to experimentally demonstrate an isoform specific

494 function for Eno3 in cell survival during EMT. This is consistent with the kinetically more active
495 muscle specific Eno3 regulating energy-intensive migratory behavior of cancer cells.
496 Comparison of our model predictions against CRISPR knockout gene essentiality scores from
497 cancer cell lines revealed a significant correlation. Interestingly, single-cell knockout simulations
498 were more correlated with CRISPR-Cas9 gene knockout essentiality data than models derived
499 from bulk omics data. CRISPR-Cas9 essentiality screening is a promising high-throughput
500 approach to determine the contribution of individual genes on cell viability. The correlation
501 between our single-cell knockout simulations and CRISPR-Cas9 knockout essentiality data
502 suggests that our model captures vulnerabilities during EMT. In addition to Eno3, we found that
503 glutaminase (FTCD), 4-hydroxyphenylpyruvate oxidoreductase (HPD),
504 adenosylhomocysteinase (AHCY), and phosphatidylserine synthase (PTDSS1) to be novel
505 reactions that have no literature backing but have negative CERES Scores (i.e. impacts
506 viability) in NSCLC cancer cell lines. The reactions prioritized by our model are strong
507 candidates for drug development because they reduce cell growth in cells from later timepoints
508 (mesenchymal/metastatic-like) relative to earlier ones (epithelial/benign-like). In addition, our
509 model predicted ATP-Citrate lyase (ACLY) to be essential in mesenchymal-like cells. ACLY has
510 been implicated as a crucial metabolic enzyme that facilitates cancer progression and its
511 upregulation is associated with poor patient prognosis ([Migita et al., 2008](#)).

512 In summary, we present a computational model that captures metabolic activity and
513 gene essentiality during EMT. Our modeling approach can be applied to study metabolism at a
514 single-cell resolution and can capture the heterogeneity of other critical biological processes,
515 including tissue differentiation and development of disease states.

516 References

- 517 1. Pastushenko, I., & Blanpain, C. (2019). EMT Transition States during Tumor Progression and
518 Metastasis. *Trends in Cell Biology*, 29(3), 212–226.
- 519 2. Padua, D., & Massagué, J. (2009). Roles of TGFbeta in metastasis. *Cell Research*, 19(1), 89–
520 102.
- 521 3. Ramesh, V., Brabletz, T., & Ceppi, P. (2020). Targeting EMT in cancer with repurposed metabolic
522 inhibitors. *Trends in Cancer*.
- 523 4. Vander Heiden, M. G., Cantley, L. C., & Thompson, C. B. (2009). Understanding the Warburg
524 effect: the metabolic requirements of cell proliferation. *Science*, 324(5930), 1029–1033.
- 525 5. Pålsson-McDermott, E. M., & O'Neill, L. A. J. (2020). Targeting immunometabolism as an anti-
526 inflammatory strategy. *Cell Research*, 30(4), 300–314.
- 527 6. Orth, J. D., Thiele, I., & Palsson, B. Ø. (2010). What is flux balance analysis? *Nature*
528 *Biotechnology*, 28(3), 245–248.
- 529 7. Oruganty, K., Campit, S. E., Mamde, S., Lyssiotis, C. A., & Chandrasekaran, S. (2020). Common
530 biochemical properties of metabolic genes recurrently dysregulated in tumors. *Cancer &*
531 *Metabolism*, 8, 5.
- 532 8. Yizhak, K., Gaude, E., Le Dévédec, S., Waldman, Y. Y., Stein, G. Y., van de Water, B., Frezza,
533 C., & Ruppin, E. (2014). Phenotype-based cell-specific metabolic modeling reveals metabolic
534 liabilities of cancer. *Elife*, 3, e03641.
- 535 9. Nilsson, A., Haanstra, J. R., Engqvist, M., Gerding, A., Bakker, B. M., Klingmüller, U., ... &
536 Nielsen, J. (2020). Quantitative analysis of amino acid metabolism in liver cancer links glutamate
537 excretion to nucleotide synthesis. *Proceedings of the National Academy of Sciences*, 117(19),
538 10294-10304.
- 539 10. Nelson, B. S., Lin, L., Kremer, D. M., Sousa, C. M., Cotta-Ramusino, C., Myers, A., Ramos, J.,
540 Gao, T., Kovalenko, I., Wilder-Romans, K., Dresser, J., Davis, M., Lee, H.-J., Nwosu, Z. C.,
541 Campit, S., Mashadova, O., Nicolay, B. N., Tolstyka, Z. P., Halbrook, C. J., ... Lyssiotis, C. A.
542 (2020). Tissue of origin dictates GOT1 dependence and confers synthetic lethality to
543 radiotherapy. *Cancer & Metabolism*, 8, 1.
- 544 11. Hecker, L., Vittal, R., Jones, T., Jagirdar, R., Luckhardt, T. R., Horowitz, J. C., Pennathur, S.,
545 Martinez, F. J., & Thannickal, V. J. (2009). NADPH oxidase-4 mediates myofibroblast activation
546 and fibrogenic responses to lung injury. *Nature Medicine*, 15(9), 1077–1081.
- 547 12. Keshamouni, V. G., Jagtap, P., Michailidis, G., Strahler, J. R., Kuick, R., Reka, A. K., Papoulias,
548 P., Krishnapuram, R., Srirangam, A., Standiford, T. J., Andrews, P. C., & Omenn, G. S. (2009).
549 Temporal quantitative proteomics by iTRAQ 2D-LC-MS/MS and corresponding mRNA expression
550 analysis identify post-transcriptional modulation of actin-cytoskeleton regulators during TGF-beta-
551 induced epithelial-mesenchymal transition. *Journal of Proteome Research*, 8(1), 35–47.
- 552 13. Keshamouni, V. G., Michailidis, G., Grasso, C. S., Anthwal, S., Strahler, J. R., Walker, A.,
553 Arenberg, D. A., Reddy, R. C., Akulapalli, S., Thannickal, V. J., Standiford, T. J., Andrews, P. C.,
554 & Omenn, G. S. (2006). Differential protein expression profiling by iTRAQ-2DLC-MS/MS of lung
555 cancer cells undergoing epithelial-mesenchymal transition reveals a migratory/invasive
556 phenotype. *Journal of Proteome Research*, 5(5), 1143–1154.
- 557 14. Lu, C., Sidoli, S., Kulej, K., Ross, K., Wu, C. H., & Garcia, B. A. (2019). Coordination between
558 TGF-β cellular signaling and epigenetic regulation during epithelial to mesenchymal transition.
559 *Epigenetics & Chromatin*, 12(1), 11.
- 560 15. Law, C. W., Chen, Y., Shi, W., & Smyth, G. K. (2014). voom: precision weights unlock linear
561 model analysis tools for RNA-seq read counts. *Genome Biology*, 15(2), 1–17.
- 562 16. Cook, D. P., & Vanderhyden, B. C. (2020). Context specificity of the EMT transcriptional
563 response. *Nature Communications*, 11(1), 2142.
- 564 17. Van Dijk, D., Sharma, R., Nainys, J., Yim, K., Kathail, P., Carr, A. J., ... & Pe'er, D. (2018).
565 Recovering gene interactions from single-cell data using data diffusion. *Cell*, 174(3), 716-729.
- 566 18. Duarte, N. C., Becker, S. A., Jamshidi, N., Thiele, I., Mo, M. L., Vo, T. D., Srivas, R., & Palsson,
567 B. Ø. (2007). Global reconstruction of the human metabolic network based on genomic and
568 bibliomic data. *Proceedings of the National Academy of Sciences of the United States of*
569 *America*, 104(6), 1777–1782.

- 570 19. Zur, H., Ruppin, E., & Shlomi, T. (2010). iMAT: an integrative metabolic analysis tool.
571 *Bioinformatics*, 26(24), 3140–3142.
- 572 20. Shen, F., Boccutto, L., Pauly, R., Srikanth, S., & Chandrasekaran, S. (2019). Genome-scale
573 network model of metabolism and histone acetylation reveals metabolic dependencies of histone
574 deacetylase inhibitors. *Genome biology*, 20(1), 1-15.
- 575 21. Lewis, N. E., Hixson, K. K., Conrad, T. M., Lerman, J. A., Charusanti, P., Polpitiya, A. D., Adkins,
576 J. N., Schramm, G., Purvine, S. O., Lopez-Ferrer, D., Weitz, K. K., Eils, R., König, R., Smith, R.
577 D., & Palsson, B. Ø. (2010). Omic data from evolved E. coli are consistent with computed optimal
578 growth from genome-scale models. *Molecular Systems Biology*, 6, 390.
- 579 22. Liberzon, A., Birger, C., Thorvaldsdóttir, H., Ghandi, M., Mesirov, J. P., & Tamayo, P. (2015). The
580 molecular signatures database hallmark gene set collection. *Cell systems*, 1(6), 417-425.
- 581 23. Vasaikar, S. V., Deshmukh, A. P., den Hollander, P., Addanki, S., Kuburich, N. A., Kudaravalli, S.,
582 ... & Mani, S. A. (2021). EMTome: A resource for pan-cancer analysis of epithelial-mesenchymal
583 transition genes and signatures. *British journal of cancer*, 124(1), 259-269.
- 584 24. Pacini, C., Dempster, J. M., Boyle, I., Gonçalves, E., Najgebauer, H., Karakoc, E., van der Meer,
585 D., Barthorpe, A., Lightfoot, H., Jaaks, P., McFarland, J. M., Garnett, M. J., Tsherniak, A., & Iorio,
586 F. (2021). Integrated cross-study datasets of genetic dependencies in cancer. *Nature*
587 *Communications*, 12(1), 1661.
- 588 25. Barretina, J., Caponigro, G., Stransky, N., Venkatesan, K., Margolin, A. A., Kim, S., Wilson, C. J.,
589 Lehar, J., Kryukov, G. V., Murray, L., Morrissey, M. P., Sellers, W. R., Schlegel, R., & Garraway,
590 L. A. (2012). 22 The Cancer Cell Line Encyclopedia - Using Preclinical Models to Predict
591 Anticancer Drug Sensitivity. In *European Journal of Cancer* (Vol. 48, pp. S5–S6). doi:
592 10.1016/s0959-8049(12)70726-8
- 593 26. O'Brien, E. J., Monk, J. M., & Palsson, B. O. (2015). Using genome-scale models to predict
594 biological capabilities. *Cell*, 161(5), 971-987.
- 595 27. Vander Heiden, M. G., Cantley, L. C., & Thompson, C. B. (2009). Understanding the Warburg
596 effect: the metabolic requirements of cell proliferation. *science*, 324(5930), 1029-1033.
- 597 28. Jia, D., Park, J. H., Kaur, H., Jung, K. H., Yang, S., Tripathi, S., Galbraith, M., Deng, Y., Jolly, M.
598 K., Kaiparettu, B. A., Onuchic, J. N., & Levine, H. (2021). Towards decoding the coupled
599 decision-making of metabolism and epithelial-to-mesenchymal transition in cancer. *British Journal*
600 *of Cancer*. doi: 10.1038/s41416-021-01385-y
- 601 29. Wei, Q., Qian, Y., Yu, J., & Wong, C. C. (2020). Metabolic rewiring in the promotion of cancer
602 metastasis: mechanisms and therapeutic implications. *Oncogene*, 39(39), 6139–6156.
- 603 30. Campit, S. E., Meliki, A., Youngson, N. A., & Chandrasekaran, S. (2020). Nutrient Sensing by
604 Histone Marks: Reading the Metabolic Histone Code Using Tracing, Omics, and
605 Modeling. *BioEssays*, 42(9), 2000083.
- 606 31. Song, Y., Luo, Q., Long, H., Hu, Z., Que, T., Zhang, X. 'an, Li, Z., Wang, G., Yi, L., Liu, Z., Fang,
607 W., & Qi, S. (2014). Alpha-enolase as a potential cancer prognostic marker promotes cell growth,
608 migration, and invasion in glioma. *Molecular Cancer*, 13, 65.
- 609 32. Zhao, M., Fang, W., Wang, Y., Guo, S., Shu, L., Wang, L., Chen, Y., Fu, Q., Liu, Y., Hua, S., Fan,
610 Y., Liu, Y., Deng, X., Luo, R., Mei, Z., Jiang, Q., & Liu, Z. (2015). Enolase-1 is a therapeutic target
611 in endometrial carcinoma. *Oncotarget*, 6(17), 15610–15627.
- 612 33. Hou, X.-M., Yuan, S.-Q., Zhao, D., Liu, X.-J., & Wu, X.-A. (2019). LDH-A promotes malignant
613 behavior via activation of epithelial-to-mesenchymal transition in lung adenocarcinoma.
614 *Bioscience Reports*, 39(1). doi: 10.1042/BSR20181476
- 615 34. Zhang, Y., Lin, S., Chen, Y., Yang, F., & Liu, S. (2018). LDH-A promotes epithelial-mesenchymal
616 transition by upregulating ZEB2 in intestinal-type gastric cancer. *OncoTargets and Therapy*, 11,
617 2363–2373.
- 618 35. Menendez, J. A., Vellon, L., Mehmi, I., Oza, B. P., Ropero, S., Colomer, R., & Lupu, R. (2004).
619 Inhibition of fatty acid synthase (FAS) suppresses HER2/neu (erbB-2) oncogene overexpression
620 in cancer cells. *Proceedings of the National Academy of Sciences of the United States of*
621 *America*, 101(29), 10715–10720.
- 622 36. Pizer, E. S., Wood, F. D., Heine, H. S., Romantsev, F. E., Pasternack, G. R., & Kuhajda, F. P.
623 (1996). Inhibition of fatty acid synthesis delays disease progression in a xenograft model of
624 ovarian cancer. *Cancer Research*, 56(6), 1189–1193.

- 625 37. Xu, X., Chen, B., Zhu, S., Zhang, J., He, X., Cao, G., & Chen, B. (2019). Hyperglycemia promotes
626 Snail-induced epithelial–mesenchymal transition of gastric cancer via activating ENO1
627 expression. *Cancer Cell International*, 19(1), 1–12.
- 628 38. Liu, M., Quek, L.-E., Sultani, G., & Turner, N. (2016). Epithelial-mesenchymal transition induction
629 is associated with augmented glucose uptake and lactate production in pancreatic ductal
630 adenocarcinoma. *Cancer & Metabolism*, 4, 19.
- 631 39. Birsoy, K., Wang, T., Chen, W. W., Freinkman, E., Abu-Remaileh, M., & Sabatini, D. M. (2015).
632 An Essential Role of the Mitochondrial Electron Transport Chain in Cell Proliferation Is to Enable
633 Aspartate Synthesis. *Cell*, 162(3), 540–551.
- 634 40. Alkan, H. F., Walter, K. E., Luengo, A., Madreiter-Sokolowski, C. T., Stryeck, S., Lau, A. N., Al-
635 Zoughbi, W., Lewis, C. A., Thomas, C. J., Hoefler, G., Graier, W. F., Madl, T., Vander Heiden, M.
636 G., & Bogner-Strauss, J. G. (2018). Cytosolic Aspartate Availability Determines Cell Survival
637 When Glutamine Is Limiting. *Cell Metabolism*, 28(5), 706–720.e6.
- 638 41. Sullivan, L. B., Gui, D. Y., Hosios, A. M., Bush, L. N., Freinkman, E., & Vander Heiden, M. G.
639 (2015). Supporting Aspartate Biosynthesis Is an Essential Function of Respiration in Proliferating
640 Cells. *Cell*, 162(3), 552–563.
- 641 42. Yang, L., Venneti, S., & Nagrath, D. (2017). Glutaminolysis: a hallmark of cancer metabolism.
642 *Annual review of biomedical engineering*, 19, 163-194.
- 643 43. Cacace, A., Sboarina, M., Vazeille, T., & Sonveaux, P. (2017). Glutamine activates STAT3 to
644 control cancer cell proliferation independently of glutamine metabolism. *Oncogene*, 36(15), 2074-
645 2084.
- 646 44. Yang, L., Moss, T., Mangala, L. S., Marini, J., Zhao, H., Wahlig, S., ... & Nagrath, D. (2014).
647 Metabolic shifts toward glutamine regulate tumor growth, invasion and bioenergetics in ovarian
648 cancer. *Molecular systems biology*, 10(5), 728.
- 649 45. Sellers, K., Fox, M. P., li, M. B., Slone, S. P., Higashi, R. M., Miller, D. M., Wang, Y., Yan, J.,
650 Yuneva, M. O., Deshpande, R., Lane, A. N., & Fan, T. W.-M. (2015). Pyruvate carboxylase is
651 critical for non–small-cell lung cancer proliferation. *The Journal of Clinical Investigation*, 125(2),
652 687–698.
- 653 46. Fu, X.-G., Deng, J., Xu, W.-J., Chen, J.-Y., Sun, J., & Deng, H. (2020). Histidine decarboxylase-
654 expressing PMN-MDSC-derived TGF-β1 promotes the epithelial-mesenchymal transition of
655 metastatic lung adenocarcinoma. *International Journal of Clinical and Experimental Pathology*,
656 13(6), 1361–1371.
- 657 47. Meyers, R. M., Bryan, J. G., McFarland, J. M., Weir, B. A., Sizemore, A. E., Xu, H., ... &
658 Tsherniak, A. (2017). Computational correction of copy number effect improves specificity of
659 CRISPR–Cas9 essentiality screens in cancer cells. *Nature genetics*, 49(12), 1779-1784.
- 660 48. Migita, T., Narita, T., Nomura, K., Miyagi, E., Inazuka, F., Matsuura, M., ... & Ishikawa, Y. (2008).
661 ATP citrate lyase: Activation and therapeutic implications in non–small cell lung cancer. *Cancer*
662 *research*, 68(20), 8547-8554.

663 Data and software availability statement

664 Bulk transcriptomics data was obtained from GSE17708 and GSE17518. Bulk proteomics data
665 was obtained from Keshamouni et al., 2006 and Lu et al., 2019. Single-cell EMT transcriptomics
666 data was obtained from GSE147405.

667

668 All COBRA data and meta-analyses performed can be found in the supplementary table.

669

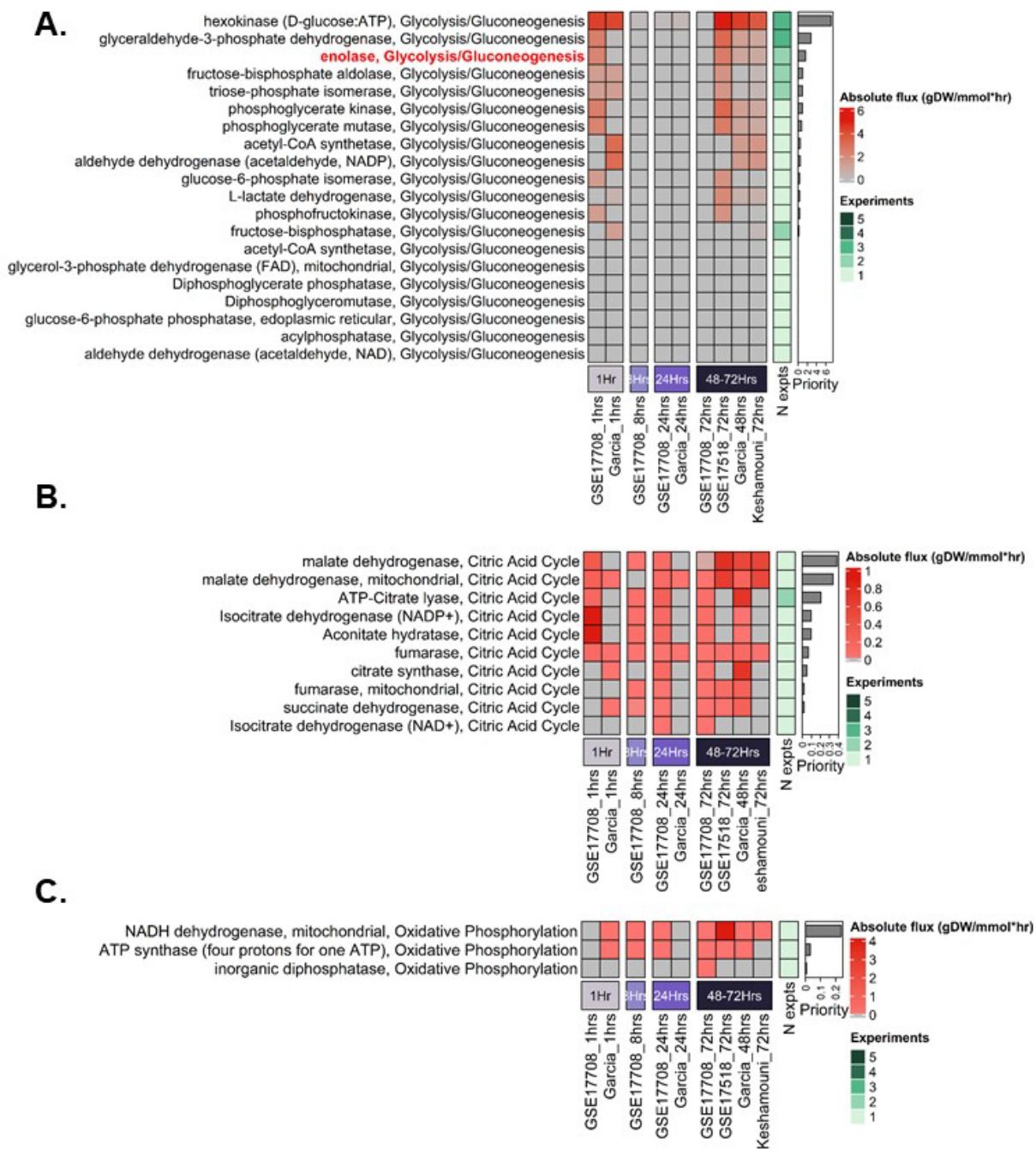
670 All scripts used to analyze these datasets can be found in this [GitHub repository](#).

671

672

673

674 Main Figures and Data Tables



675
676

677 **Figure 1. A549 metabolism is predicted to be overactive during the early and late phases**
678 **of EMT.**

- 679 A. Reactions are sorted based on the priority score, which is a function of the number of
680 studies with significant metabolic genes that encode the reaction and the effect size (Z-
681 score or log₂ fold change). The metabolic fluxes were simulated using the RECON1
682 human metabolic reconstruction. Several metabolic reactions within the
683 Glycolysis/Gluconeogenesis metabolic subsystem are overactive in the earlier stages
684 (1hr) and late stages (48-72hrs) of EMT, based on the absolute value of the metabolic
685 fluxes predicted by constraint-based modeling. The top 5 reactions in the
686 Glycolysis/Gluconeogenesis subsystem have at least two studies supporting the flux
687 predictions. Enolase is bolded as it was prioritized for experimental validation.
- 688 B. Metabolic reactions within the Citric Acid Cycle are predicted to have more uniform
689 activity across all time points relative to control (unconstrained flux distribution) and have
690 lower priority scores compared to glycolysis.
- 691 C. Metabolic reactions within the Oxidative Phosphorylation metabolic subsystem are also
692 predicted to have more uniform activity relative to control across all time points.

693

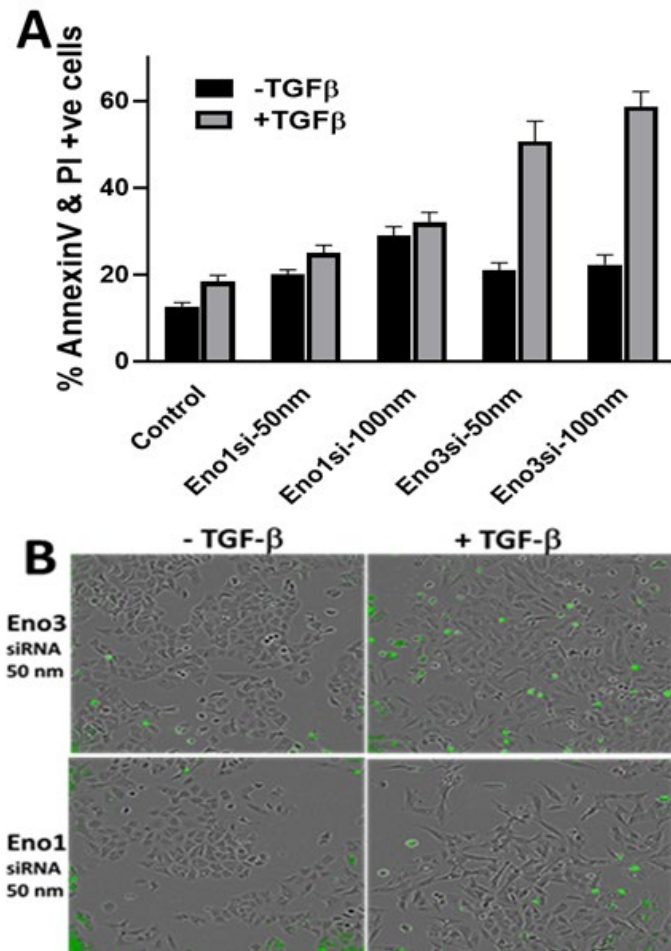
694



695

696

697 **Figure 2. A global view of cancer growth sensitivity to metabolic reaction knockout**
698 **during EMT.** Normalized KO Growth Scores closer to a value of -1 confer a decrease in growth
699 relative upon simulated reaction knockout relative to the control (an unconstrained metabolic
700 reconstruction growth rate). Reactions are sorted based on priority scores.
701 The barplots (inset) show the distribution of lethal reactions (Growth Score < 0) for three
702 timepoints 1 hour, 24 hours, and 48-72 hours after TGF- β induction across all experiments in 3
703 time points. Reactions with red and bold text were predicted to be highly sensitive to knockout
704 and were prioritized for downstream analyses with CERES essentiality scores.
705



706
707

708 **Figure 3. siRNA-mediated inhibition of Eno3, but not Eno1, triggers apoptosis in A549**
709 **cells undergoing EMT after 72 h TGF- β treatment.**

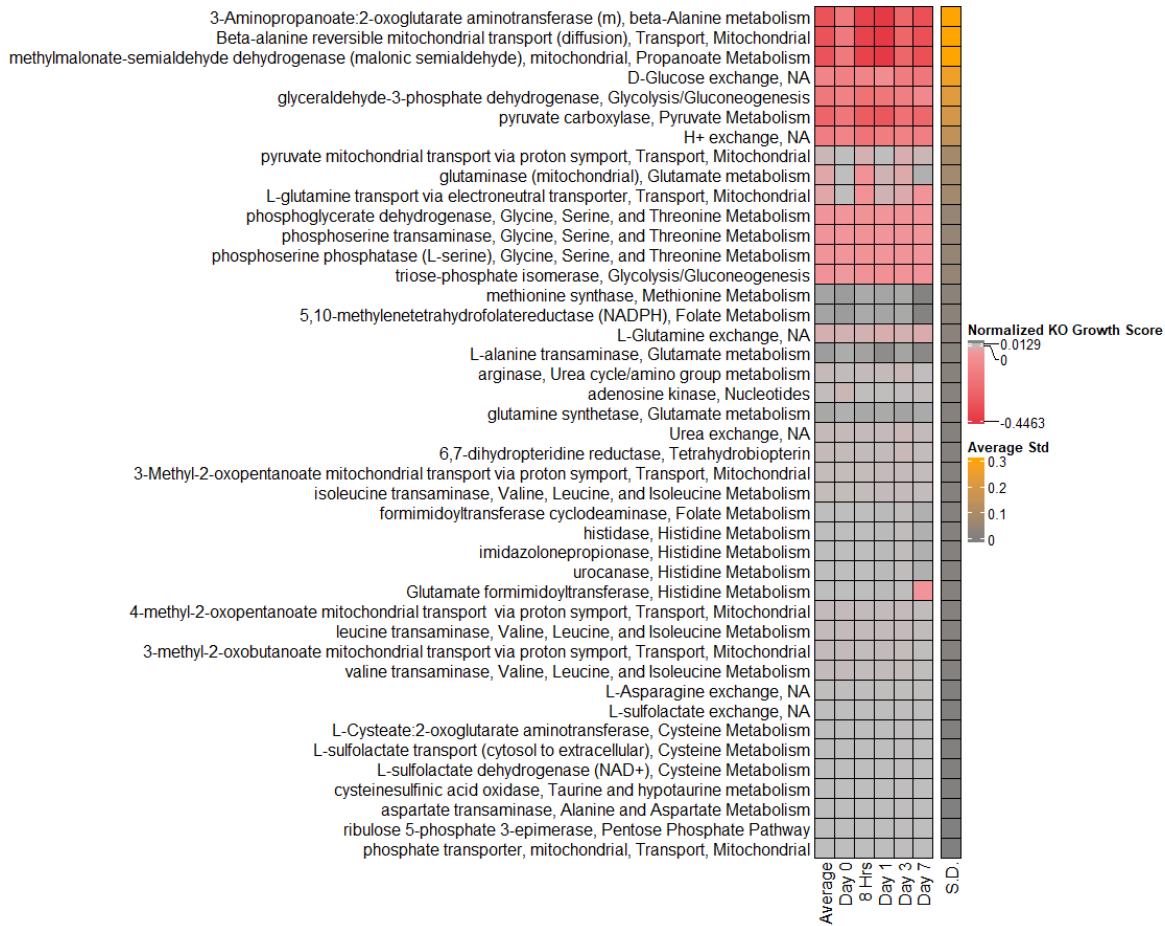
- 710 A. Apoptosis is assessed by the percentage of AnnexinV & PI positive cells by Flow
711 cytometry.
712 B. Caspase activation is measured using a caspase8 specific substrate that fluoresces
713 after caspase 8-mediated cleavage.

714

715

716

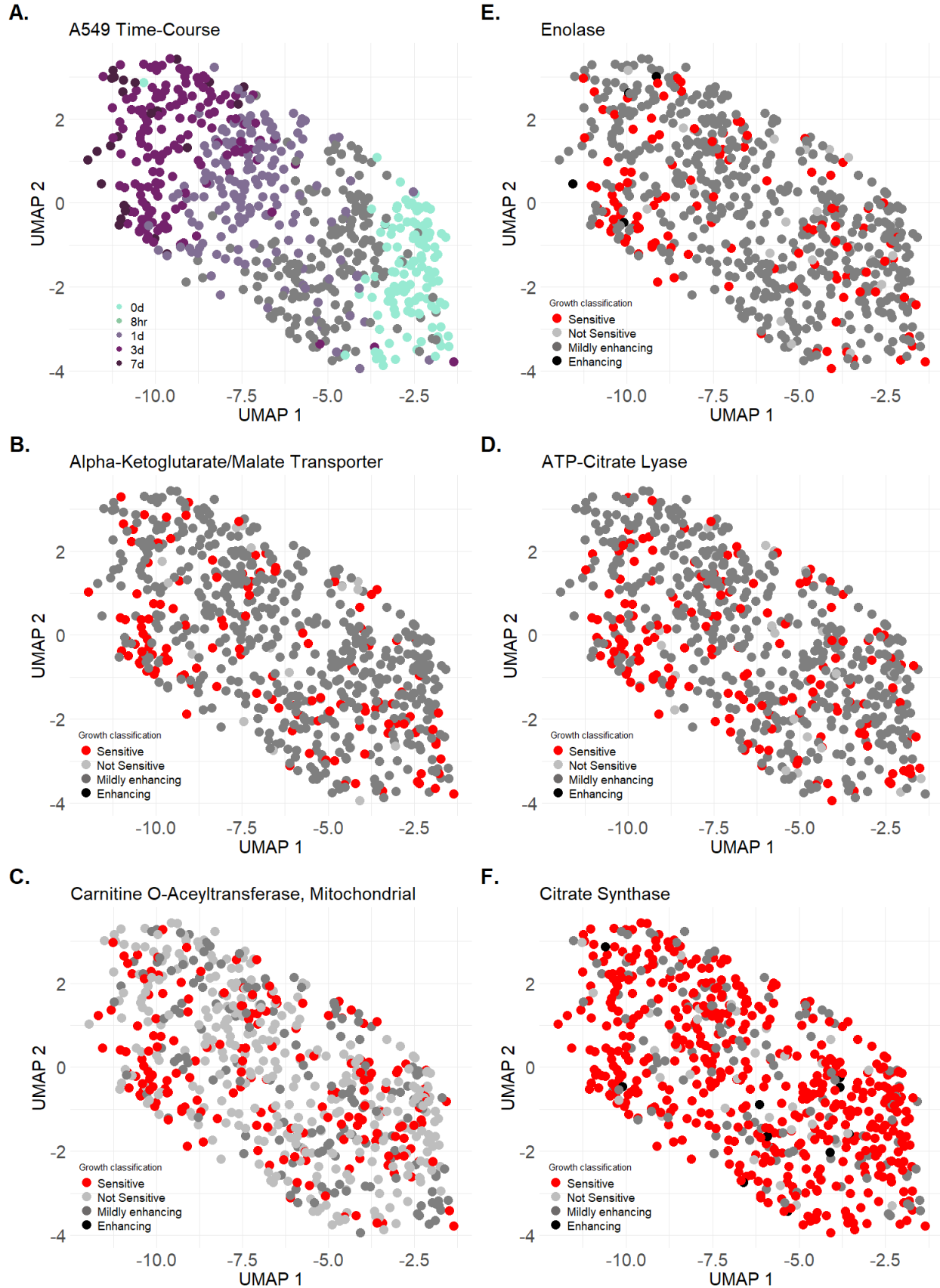
717



718

719

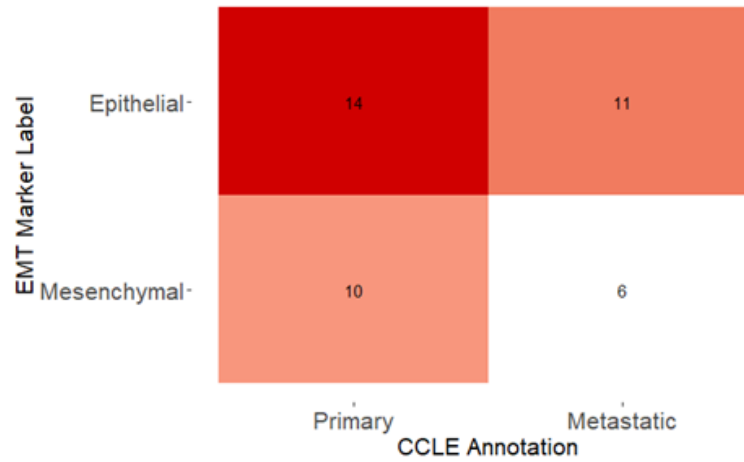
720 **Figure 4. Single-cell COBRA reaction knockout analysis is consistent with results from**
721 **bulk studies.** Reaction knockout growth rates for the top 40 most variable reactions are shown
722 in the heatmap. Column1 shows averaged data across all cells in the single-cell simulations,
723 and data from cells grouped by time points are shown in subsequent columns (day 0, 8 hrs, day
724 1, day 3 and day 7). This list contains many reactions that were also found to be sensitive upon
725 knockout in bulk studies (Table 1).
726



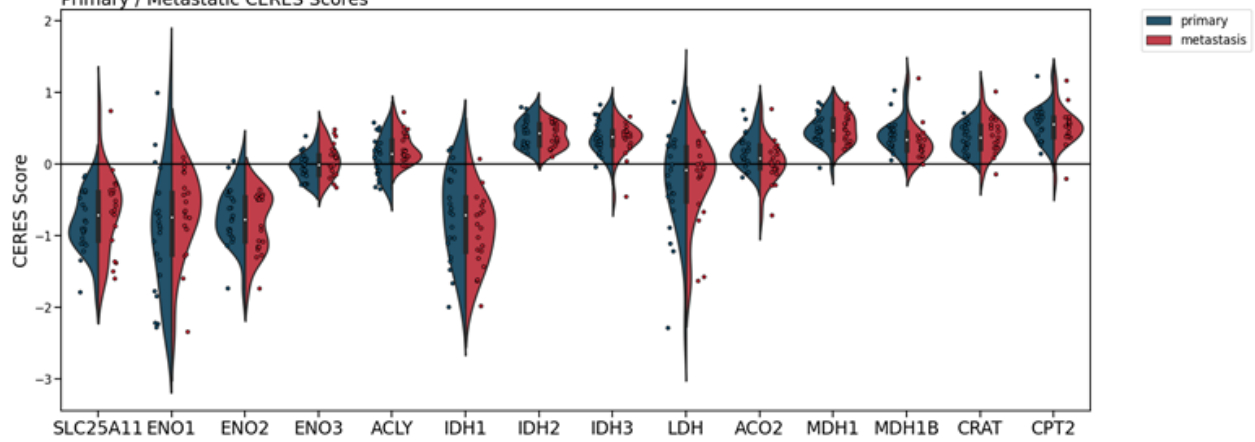
728 **Figure 5. Visualization of Single-cell COBRA reaction knockout data.**

729 **A.** Shown is the UMAP visualization of the temporal trajectory of cells induced with TGF-B.
730 **B – F.** Single-cell knockout growth rates were overlaid onto a UMAP embedding for A549 TGF-
731 B single cell data. Growth rates were scaled from 0 to 1, where 1 indicates no change in growth
732 rate between the cancer cell and control, while 0 indicates cell death in the cancer cell relative
733 to control. Selected single-cell growth rate profiles for reactions that were sensitive in bulk
734 reaction knockout simulations are shown in B-E. Growth scores (g.s.) were discretized into
735 sensitive (g.s. < 0; red), not sensitive (g.s. = 0; light gray), mildly enhancing (0 < g.s. < 0.3; dark
736 gray) and enhancing (g.s. > 0.3; black). The citrate synthase reaction (panel F) was selected as
737 a control as it is an essential metabolic reaction, and it correctly shows sensitivity across all time
738 points.
739
740

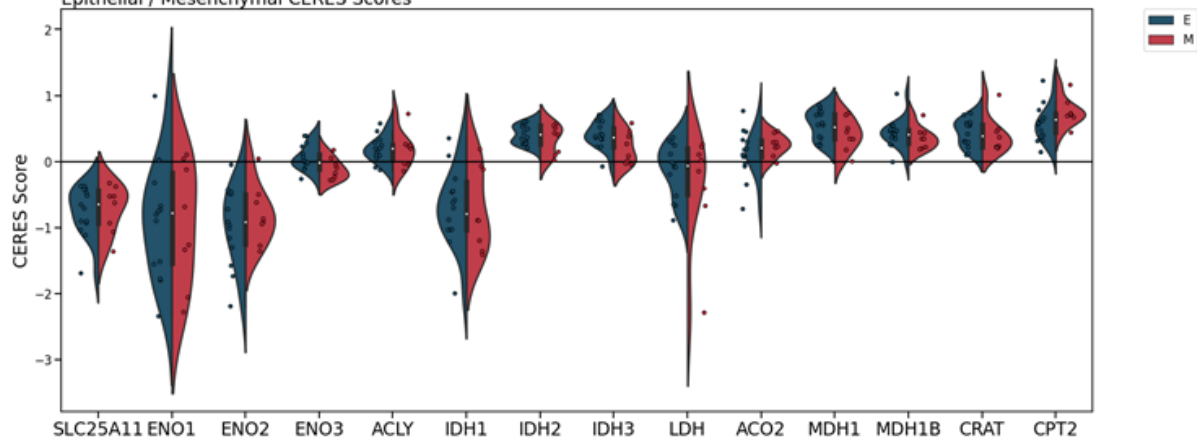
A.



B. Primary / Metastatic CERES Scores



C. Epithelial / Mesenchymal CERES Scores



742 **Figure 6. COBRA-prioritized NSCLC CERES Scores reveal metabolic vulnerabilities**
743 **during EMT.**

- 744 A. Frequency matrix for comparing the Cancer Cell Line Encyclopedia (CCLE)
745 primary/metastatic annotations against our Epithelial/Mesenchymal annotations based
746 on MSigDB and EMTome signatures. Cells from the CCLE were classified as epithelial
747 or mesenchymal based on the number of genes were up/downregulated that matched
748 the MSigDB/EMTome signatures (**Methods**).
- 749 B. Reactions predicted by COBRA to be sensitive were compared against CERES Scores.
750 Cell lines were classified as primary or metastatic, and their distributions are shown on
751 the violin plots. Overall, the average predicted growth scores and fluxes in hour 72
752 across all 5 experiments agreed with the Primary / Metastatic CERES Scores Ratios (R
753 = 0.31 and 0.2; P-value = 0.005 and 0.035 respectively; **S. Table 6 and 7**). These 10
754 metabolic genes were selected based on reactions of interest from our bulk COBRA
755 knockout profiles and single-cell flux profiles (from **Figure 2**).
- 756 C. The same analysis was repeated with the epithelial/mesenchymal annotations for
757 sensitive reactions. The predicted growth scores and fluxes from the single-cell
758 simulations (GSE147405) agreed with the Epithelial / Mesenchymal CERES Scores
759 Ratios ($R = 0.28$, p-value=0.01).
- 760

761 Main Tables and Legends

Table 1. Literature review of known and novel essential reactions predicted from both bulk and single-cell simulations.

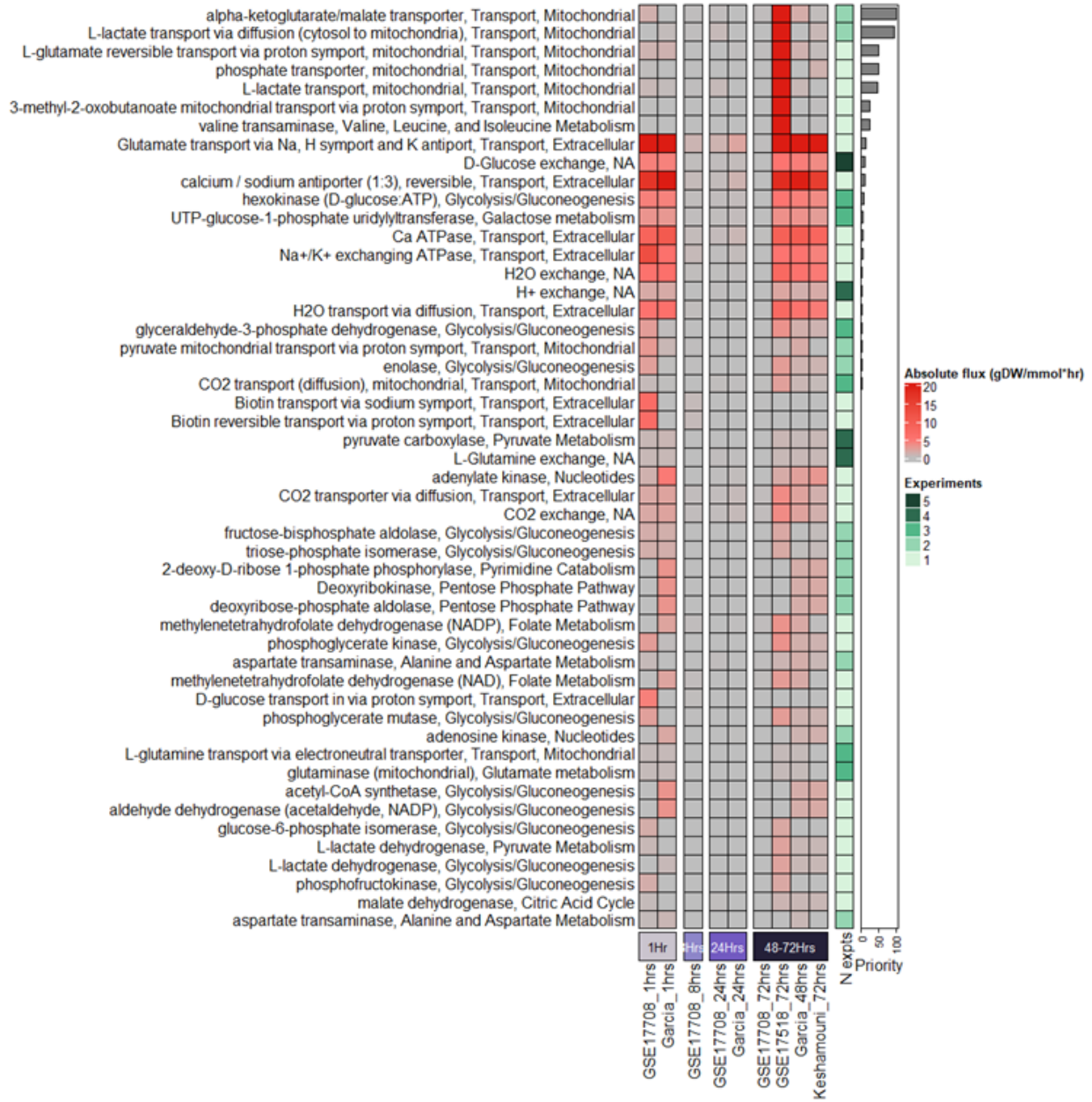
For full list of all predicted essential reactions, see **S. Table 5**.

Reaction Name	Gene-Protein-Reaction Rule	Average NSCLC CERES Score	PMID
<i>Strong evidence</i>			
			26070193
			30005601
pyruvate carboxylase	(PC)	-0.5217	25607840
			32530543
fructose-bisphosphate aldolase	(ALDOA) or (ALDOC) or (ALDOB)	-0.7012	28444969
			31358528
<i>Medium evidence</i>			
ribulose 5-phosphate 3-epimerase	(RPE)	-1.3731	32365991
triose-phosphate isomerase	(TPI1) or (TPIP2)	-1.1346	27908734
formimidoyltransferase			
cyclodeaminase	(FTCD)	-0.0908	30784016
glyceraldehyde-3-phosphate dehydrogenase	(GAPDH) or (GAPDHS)	-0.7870	27878251
UTP-glucose-1-phosphate uridylyltransferase	(UGP2)	-0.2952	31243371
ATP-Citrate lyase	(ACLY)	-0.7807	23807225
acetone mitochondrial transport via proton symport	(SLC16A1)	-0.0556	31371390
aspartate transaminase	(GOT2)	-0.3341	23535601
<i>Novel predictions</i>			
glutaminase (mitochondrial)	(FTCD)	-0.0908	
4-Hydroxyphenylpyruvate:oxygen oxidoreductase	(HPD)	-0.0390	
adenosylhomocysteinase	(AHCY) or (AHCYL1)	-0.6535	
enolase	(ENO1) or (ENO3) or (ENO2)	-0.0015	
Phosphatidylserine synthase homo sapiens	(PTDSS1)	-0.2514	

762

763

764

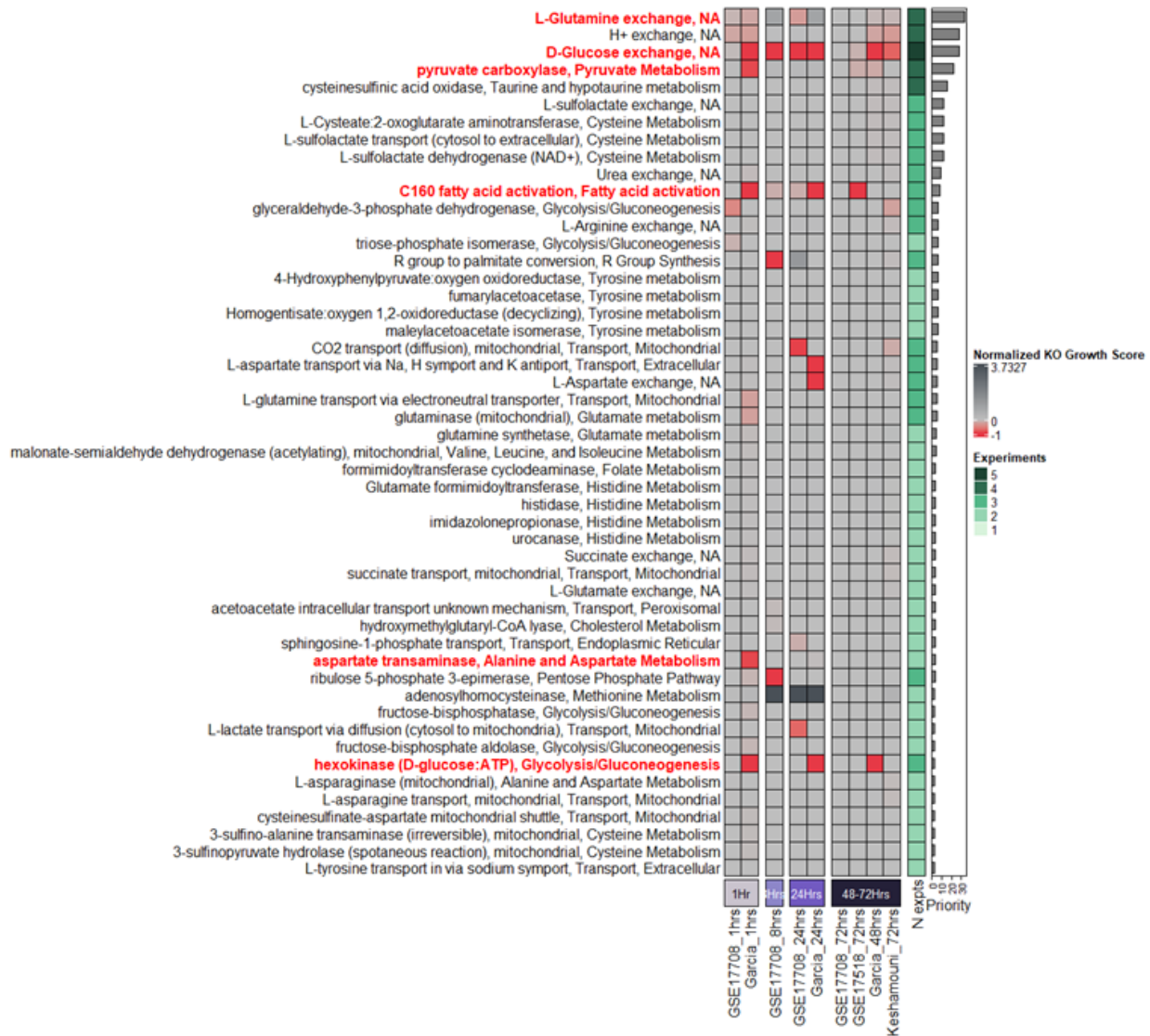


765
766

767 **Supplementary Figure 1. The top 50 reactions that are predicted to be overactive are**
768 **ranked by priority score. (Related to figure 1)**

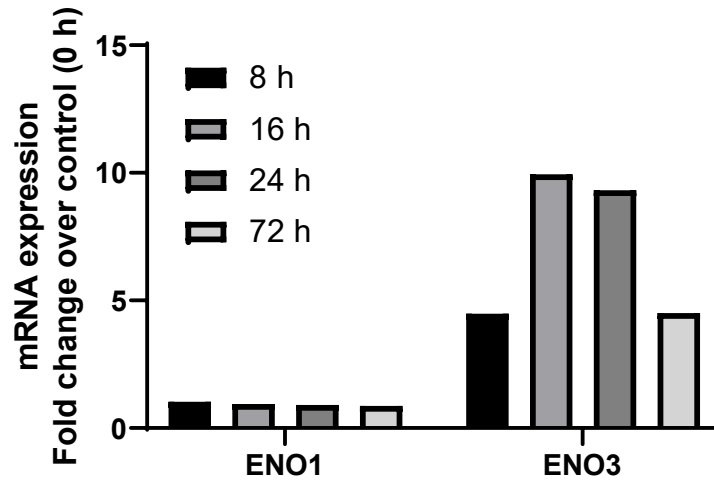
769 The priority score is a function of the number of studies with significant metabolic genes that
770 encode the reaction and the effect size (Z-score or log2 fold change). The metabolic fluxes were
771 simulated using the RECON1 metabolic reconstruction. Several EMT associated metabolic
772 reactions predicted by our model such as Glycolysis/Gluconeogenesis, Glutamine metabolism
773 and Nucleic acid metabolism are commonly dysregulated in cancer.

774
775
776



777
778
779

780 **Supplementary Figure 2. Top 50 reactions ranked by priority score predicted to be**
781 **sensitive to reaction KO. (related to figure 2)** The heatmap shows the top 50 reactions
782 ranked by priority score predicted to reduce A549 growth rate upon reaction knockout in
783 RECON1 in all bulk experiments. In contrast, Figure 2 focuses on reactions sensitive in specific
784 EMT stages and studies, while this sensitivity profile shows the top 50 reactions by priority
785 score. Eight nutrient exchange reactions including glucose and aspartate exchange reactions
786 were predicted to have a negative impact on growth following knockout at different stages of
787 EMT. Glutamine exchange interestingly decreased growth upon KO during early and late EMT
788 timepoints but not in intermediate time-point (24hrs). Hexokinase and C100 fatty acid activation
789 were predicted to be essential across all time points. Pyruvate carboxylase was predicted to be
790 sensitive in early EMT (1 hour).

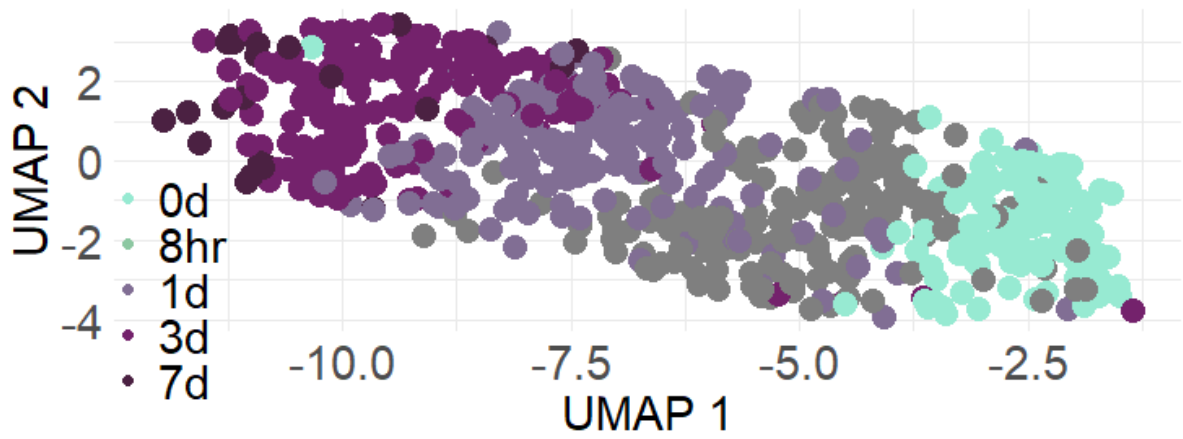


791
792

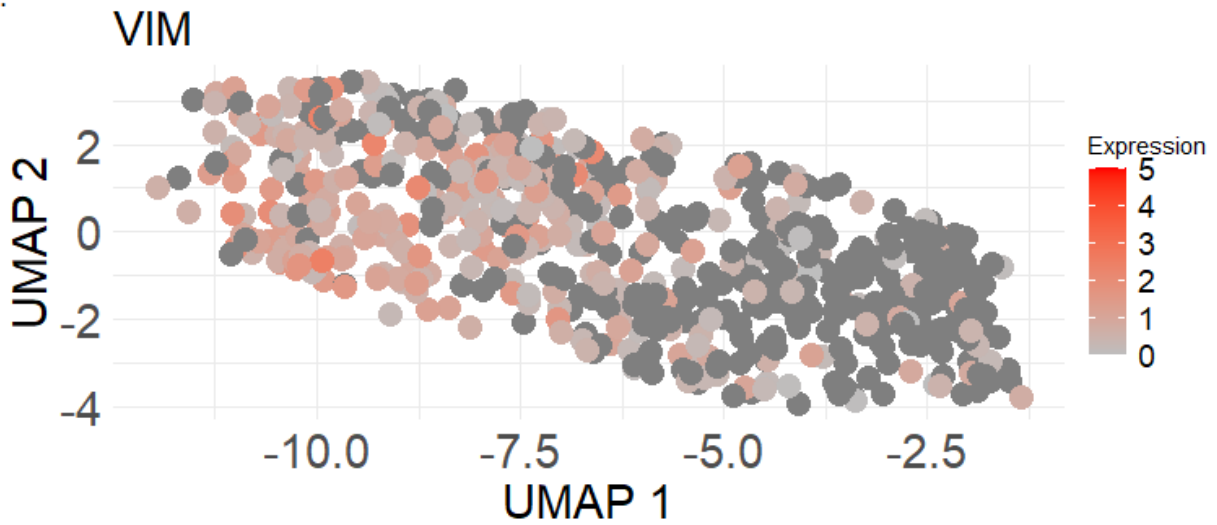
793 **Supplementary Figure 3. mRNA expression fold change of ENO1 versus ENO3 over time**
794

A.

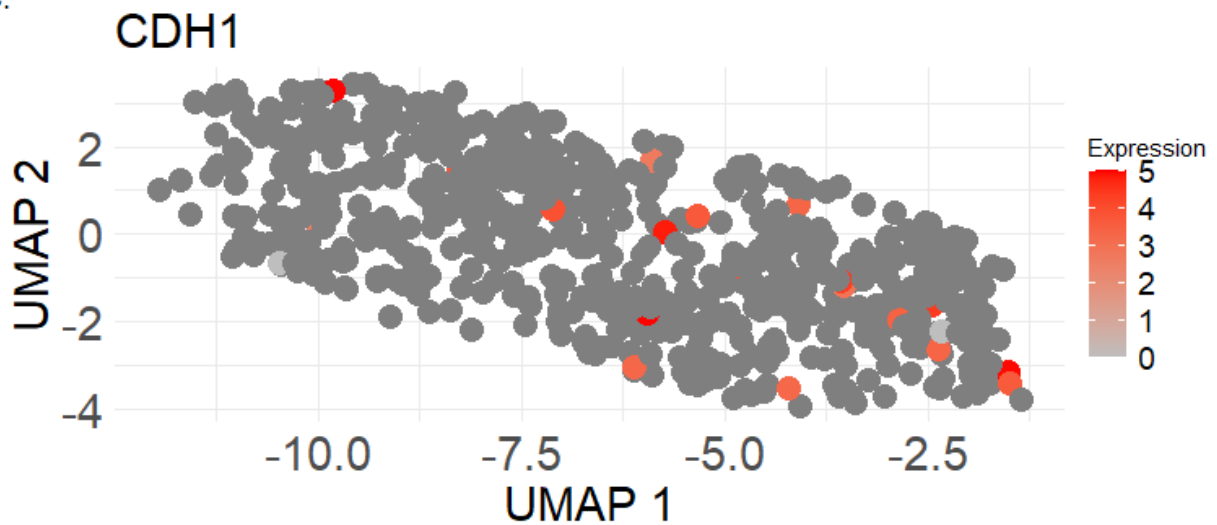
A549 Time-Course



B.

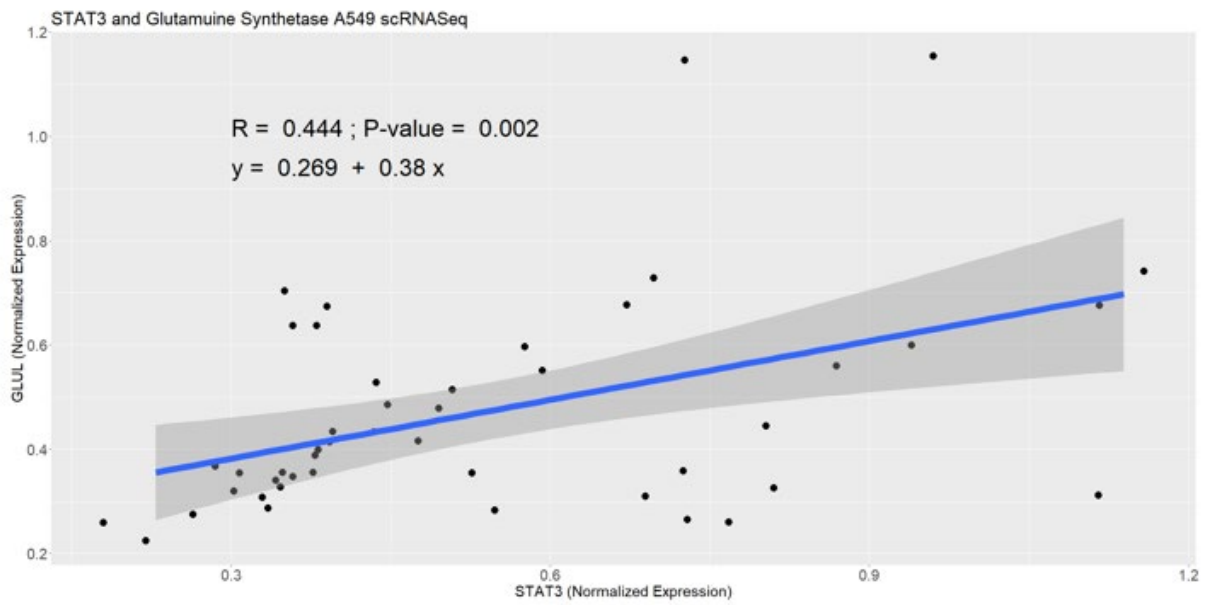


C.

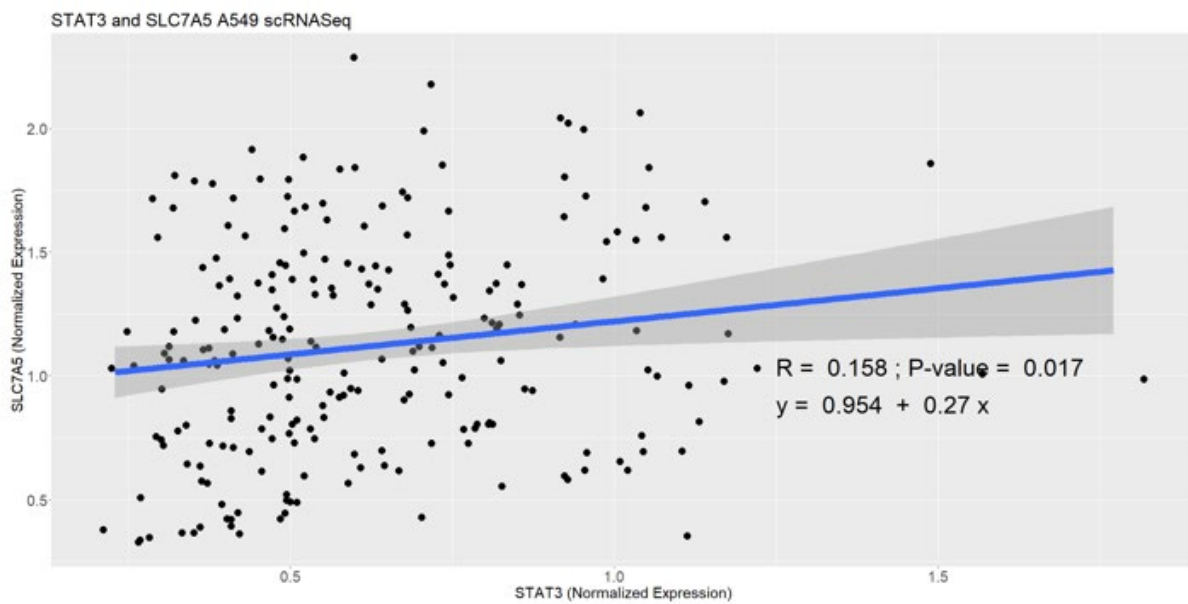


- 796 **Supplementary Figure 4. Single-cell RNASeq data of EMT biomarkers reveals cell states.**
797 A. Time-course trajectory of A549 cells induced with TGF-B.
798 B. VIM expression over time.
799 C. CDH1 expression over time.
800

A.



B.



801

802 **Supplementary Figure 5. Correlation analysis between STAT3 and glutamine metabolism-**
803 **related genes Glutamine Synthetase and glutamine transporter SLC7A5.**

- 804 A. Shown are cells that contain non-zero expression levels for both STAT3 and GLUL
805 across cells with TGF- β induction. A significant positive correlation ($R = 0.444$; P-value =
806 0.002) was observed.
- 807 B. Shown are cells that contain non-zero expression levels for both STAT3 and SLC7A5
808 across cells with TGF- β induction. A significant but weaker positive correlation ($R =$
809 0.158; P-value = 0.017) was observed.

810 References

- 811 1. Pastushenko, I., & Blanpain, C. (2019). EMT Transition States during Tumor Progression and
812 Metastasis. *Trends in Cell Biology*, 29(3), 212–226.
- 813 2. Padua, D., & Massagué, J. (2009). Roles of TGFbeta in metastasis. *Cell Research*, 19(1), 89–
814 102.
- 815 3. Ramesh, V., Brabletz, T., & Ceppi, P. (2020). Targeting EMT in cancer with repurposed metabolic
816 inhibitors. *Trends in Cancer*.
- 817 4. Vander Heiden, M. G., Cantley, L. C., & Thompson, C. B. (2009). Understanding the Warburg
818 effect: the metabolic requirements of cell proliferation. *Science*, 324(5930), 1029–1033.
- 819 5. Pålsson-McDermott, E. M., & O'Neill, L. A. J. (2020). Targeting immunometabolism as an anti-
820 inflammatory strategy. *Cell Research*, 30(4), 300–314.
- 821 6. Orth, J. D., Thiele, I., & Palsson, B. Ø. (2010). What is flux balance analysis? *Nature*
822 *Biotechnology*, 28(3), 245–248.
- 823 7. Oruganty, K., Campit, S. E., Mamde, S., Lyssiotis, C. A., & Chandrasekaran, S. (2020). Common
824 biochemical properties of metabolic genes recurrently dysregulated in tumors. *Cancer &*
825 *Metabolism*, 8, 5.
- 826 8. Yizhak, K., Gaude, E., Le Dévédec, S., Waldman, Y. Y., Stein, G. Y., van de Water, B., Frezza,
827 C., & Ruppin, E. (2014). Phenotype-based cell-specific metabolic modeling reveals metabolic
828 liabilities of cancer. *Elife*, 3, e03641.
- 829 9. Nilsson, A., Haanstra, J. R., Engqvist, M., Gerding, A., Bakker, B. M., Klingmüller, U., ... &
830 Nielsen, J. (2020). Quantitative analysis of amino acid metabolism in liver cancer links glutamate
831 excretion to nucleotide synthesis. *Proceedings of the National Academy of Sciences*, 117(19),
832 10294-10304.
- 833 10. Nelson, B. S., Lin, L., Kremer, D. M., Sousa, C. M., Cotta-Ramusino, C., Myers, A., Ramos, J.,
834 Gao, T., Kovalenko, I., Wilder-Romans, K., Dresser, J., Davis, M., Lee, H.-J., Nwosu, Z. C.,
835 Campit, S., Mashadova, O., Nicolay, B. N., Tolstyka, Z. P., Halbrook, C. J., ... Lyssiotis, C. A.
836 (2020). Tissue of origin dictates GOT1 dependence and confers synthetic lethality to
837 radiotherapy. *Cancer & Metabolism*, 8, 1.
- 838 11. Hecker, L., Vittal, R., Jones, T., Jagirdar, R., Luckhardt, T. R., Horowitz, J. C., Pennathur, S.,
839 Martinez, F. J., & Thannickal, V. J. (2009). NADPH oxidase-4 mediates myofibroblast activation
840 and fibrogenic responses to lung injury. *Nature Medicine*, 15(9), 1077–1081.
- 841 12. Keshamouni, V. G., Jagtap, P., Michailidis, G., Strahler, J. R., Kuick, R., Reka, A. K., Papoulias,
842 P., Krishnapuram, R., Srirangam, A., Standiford, T. J., Andrews, P. C., & Omenn, G. S. (2009).
843 Temporal quantitative proteomics by iTRAQ 2D-LC-MS/MS and corresponding mRNA expression
844 analysis identify post-transcriptional modulation of actin-cytoskeleton regulators during TGF-beta-
845 induced epithelial-mesenchymal transition. *Journal of Proteome Research*, 8(1), 35–47.
- 846 13. Keshamouni, V. G., Michailidis, G., Grasso, C. S., Anthwal, S., Strahler, J. R., Walker, A.,
847 Arenberg, D. A., Reddy, R. C., Akulapalli, S., Thannickal, V. J., Standiford, T. J., Andrews, P. C.,
848 & Omenn, G. S. (2006). Differential protein expression profiling by iTRAQ-2DLC-MS/MS of lung
849 cancer cells undergoing epithelial-mesenchymal transition reveals a migratory/invasive
850 phenotype. *Journal of Proteome Research*, 5(5), 1143–1154.
- 851 14. Lu, C., Sidoli, S., Kulej, K., Ross, K., Wu, C. H., & Garcia, B. A. (2019). Coordination between
852 TGF-β cellular signaling and epigenetic regulation during epithelial to mesenchymal transition.
853 *Epigenetics & Chromatin*, 12(1), 11.
- 854 15. Law, C. W., Chen, Y., Shi, W., & Smyth, G. K. (2014). voom: precision weights unlock linear
855 model analysis tools for RNA-seq read counts. *Genome Biology*, 15(2), 1–17.
- 856 16. Cook, D. P., & Vanderhyden, B. C. (2020). Context specificity of the EMT transcriptional
857 response. *Nature Communications*, 11(1), 2142.
- 858 17. Van Dijk, D., Sharma, R., Nainys, J., Yim, K., Kathail, P., Carr, A. J., ... & Pe'er, D. (2018).
859 Recovering gene interactions from single-cell data using data diffusion. *Cell*, 174(3), 716-729.
- 860 18. Duarte, N. C., Becker, S. A., Jamshidi, N., Thiele, I., Mo, M. L., Vo, T. D., Srivas, R., & Palsson,
861 B. Ø. (2007). Global reconstruction of the human metabolic network based on genomic and
862 bibliomic data. *Proceedings of the National Academy of Sciences of the United States of*
863 *America*, 104(6), 1777–1782.

- 864 19. Zur, H., Ruppin, E., & Shlomi, T. (2010). iMAT: an integrative metabolic analysis tool.
865 *Bioinformatics*, 26(24), 3140–3142.
- 866 20. Shen, F., Boccutto, L., Pauly, R., Srikanth, S., & Chandrasekaran, S. (2019). Genome-scale
867 network model of metabolism and histone acetylation reveals metabolic dependencies of histone
868 deacetylase inhibitors. *Genome biology*, 20(1), 1-15.
- 869 21. Lewis, N. E., Hixson, K. K., Conrad, T. M., Lerman, J. A., Charusanti, P., Polpitiya, A. D., Adkins,
870 J. N., Schramm, G., Purvine, S. O., Lopez-Ferrer, D., Weitz, K. K., Eils, R., König, R., Smith, R.
871 D., & Palsson, B. Ø. (2010). Omic data from evolved *E. coli* are consistent with computed optimal
872 growth from genome-scale models. *Molecular Systems Biology*, 6, 390.
- 873 22. Liberzon, A., Birger, C., Thorvaldsdóttir, H., Ghandi, M., Mesirov, J. P., & Tamayo, P. (2015). The
874 molecular signatures database hallmark gene set collection. *Cell systems*, 1(6), 417-425.
- 875 23. Vasaikar, S. V., Deshmukh, A. P., den Hollander, P., Addanki, S., Kuburich, N. A., Kudaravalli, S.,
876 ... & Mani, S. A. (2021). EMToMe: A resource for pan-cancer analysis of epithelial-mesenchymal
877 transition genes and signatures. *British journal of cancer*, 124(1), 259-269.
- 878 24. Pacini, C., Dempster, J. M., Boyle, I., Gonçalves, E., Najgebauer, H., Karakoc, E., van der Meer,
879 D., Barthorpe, A., Lightfoot, H., Jaaks, P., McFarland, J. M., Garnett, M. J., Tsherniak, A., & Iorio,
880 F. (2021). Integrated cross-study datasets of genetic dependencies in cancer. *Nature*
881 *Communications*, 12(1), 1661.
- 882 25. Barretina, J., Caponigro, G., Stransky, N., Venkatesan, K., Margolin, A. A., Kim, S., Wilson, C. J.,
883 Lehar, J., Kryukov, G. V., Murray, L., Morrissey, M. P., Sellers, W. R., Schlegel, R., & Garraway,
884 L. A. (2012). 22 The Cancer Cell Line Encyclopedia - Using Preclinical Models to Predict
885 Anticancer Drug Sensitivity. In *European Journal of Cancer* (Vol. 48, pp. S5–S6). doi:
886 10.1016/s0959-8049(12)70726-8
- 887 26. O'Brien, E. J., Monk, J. M., & Palsson, B. O. (2015). Using genome-scale models to predict
888 biological capabilities. *Cell*, 161(5), 971-987.
- 889 27. Vander Heiden, M. G., Cantley, L. C., & Thompson, C. B. (2009). Understanding the Warburg
890 effect: the metabolic requirements of cell proliferation. *science*, 324(5930), 1029-1033.
- 891 28. Jia, D., Park, J. H., Kaur, H., Jung, K. H., Yang, S., Tripathi, S., Galbraith, M., Deng, Y., Jolly, M.
892 K., Kaiparettu, B. A., Onuchic, J. N., & Levine, H. (2021). Towards decoding the coupled
893 decision-making of metabolism and epithelial-to-mesenchymal transition in cancer. *British Journal*
894 *of Cancer*. doi: 10.1038/s41416-021-01385-y
- 895 29. Wei, Q., Qian, Y., Yu, J., & Wong, C. C. (2020). Metabolic rewiring in the promotion of cancer
896 metastasis: mechanisms and therapeutic implications. *Oncogene*, 39(39), 6139–6156.
- 897 30. Song, Y., Luo, Q., Long, H., Hu, Z., Que, T., Zhang, X., 'an, Li, Z., Wang, G., Yi, L., Liu, Z., Fang,
898 W., & Qi, S. (2014). Alpha-enolase as a potential cancer prognostic marker promotes cell growth,
899 migration, and invasion in glioma. *Molecular Cancer*, 13, 65.
- 900 31. Zhao, M., Fang, W., Wang, Y., Guo, S., Shu, L., Wang, L., Chen, Y., Fu, Q., Liu, Y., Hua, S., Fan,
901 Y., Liu, Y., Deng, X., Luo, R., Mei, Z., Jiang, Q., & Liu, Z. (2015). Enolase-1 is a therapeutic target
902 in endometrial carcinoma. *Oncotarget*, 6(17), 15610–15627.
- 903 32. Hou, X.-M., Yuan, S.-Q., Zhao, D., Liu, X.-J., & Wu, X.-A. (2019). LDH-A promotes malignant
904 behavior via activation of epithelial-to-mesenchymal transition in lung adenocarcinoma.
905 *Bioscience Reports*, 39(1). doi: 10.1042/BSR20181476
- 906 33. Zhang, Y., Lin, S., Chen, Y., Yang, F., & Liu, S. (2018). LDH-A promotes epithelial-mesenchymal
907 transition by upregulating ZEB2 in intestinal-type gastric cancer. *OncoTargets and Therapy*, 11,
908 2363–2373.
- 909 34. Menendez, J. A., Vellon, L., Mehmi, I., Oza, B. P., Ropero, S., Colomer, R., & Lupu, R. (2004).
910 Inhibition of fatty acid synthase (FAS) suppresses HER2/neu (erbB-2) oncogene overexpression
911 in cancer cells. *Proceedings of the National Academy of Sciences of the United States of*
912 *America*, 101(29), 10715–10720.
- 913 35. Pizer, E. S., Wood, F. D., Heine, H. S., Romantsev, F. E., Pasternack, G. R., & Kuhajda, F. P.
914 (1996). Inhibition of fatty acid synthesis delays disease progression in a xenograft model of
915 ovarian cancer. *Cancer Research*, 56(6), 1189–1193.
- 916 36. Xu, X., Chen, B., Zhu, S., Zhang, J., He, X., Cao, G., & Chen, B. (2019). Hyperglycemia promotes
917 Snail-induced epithelial–mesenchymal transition of gastric cancer via activating ENO1
918 expression. *Cancer Cell International*, 19(1), 1–12.

- 919 37. Liu, M., Quek, L.-E., Sultani, G., & Turner, N. (2016). Epithelial-mesenchymal transition induction
920 is associated with augmented glucose uptake and lactate production in pancreatic ductal
921 adenocarcinoma. *Cancer & Metabolism*, 4, 19.
- 922 38. Birsoy, K., Wang, T., Chen, W. W., Freinkman, E., Abu-Remaileh, M., & Sabatini, D. M. (2015).
923 An Essential Role of the Mitochondrial Electron Transport Chain in Cell Proliferation Is to Enable
924 Aspartate Synthesis. *Cell*, 162(3), 540–551.
- 925 39. Alkan, H. F., Walter, K. E., Luengo, A., Madreiter-Sokolowski, C. T., Stryeck, S., Lau, A. N., Al-
926 Zoughbi, W., Lewis, C. A., Thomas, C. J., Hoefler, G., Graier, W. F., Madl, T., Vander Heiden, M.
927 G., & Bogner-Strauss, J. G. (2018). Cytosolic Aspartate Availability Determines Cell Survival
928 When Glutamine Is Limiting. *Cell Metabolism*, 28(5), 706–720.e6.
- 929 40. Sullivan, L. B., Gui, D. Y., Hosios, A. M., Bush, L. N., Freinkman, E., & Vander Heiden, M. G.
930 (2015). Supporting Aspartate Biosynthesis Is an Essential Function of Respiration in Proliferating
931 Cells. *Cell*, 162(3), 552–563.
- 932 41. Yang, L., Venneti, S., & Nagrath, D. (2017). Glutaminolysis: a hallmark of cancer metabolism.
933 *Annual review of biomedical engineering*, 19, 163-194.
- 934 42. Cacace, A., Sboarina, M., Vazeille, T., & Sonveaux, P. (2017). Glutamine activates STAT3 to
935 control cancer cell proliferation independently of glutamine metabolism. *Oncogene*, 36(15), 2074-
936 2084.
- 937 43. Yang, L., Moss, T., Mangala, L. S., Marini, J., Zhao, H., Wahlig, S., ... & Nagrath, D. (2014).
938 Metabolic shifts toward glutamine regulate tumor growth, invasion and bioenergetics in ovarian
939 cancer. *Molecular systems biology*, 10(5), 728.
- 940 44. Chang, G. C., Liu, K. J., Hsieh, C. L., Hu, T. S., Charoenfuprasert, S., Liu, H. K., ... & Shih, N. Y.
941 (2006). Identification of α -enolase as an autoantigen in lung cancer: its overexpression is
942 associated with clinical outcomes. *Clinical Cancer Research*, 12(19), 5746-5754.
- 943 45. Sellers, K., Fox, M. P., Li, M. B., Slone, S. P., Higashi, R. M., Miller, D. M., Wang, Y., Yan, J.,
944 Yuneva, M. O., Deshpande, R., Lane, A. N., & Fan, T. W.-M. (2015). Pyruvate carboxylase is
945 critical for non-small-cell lung cancer proliferation. *The Journal of Clinical Investigation*, 125(2),
946 687–698.
- 947 46. Fu, X.-G., Deng, J., Xu, W.-J., Chen, J.-Y., Sun, J., & Deng, H. (2020). Histidine decarboxylase-
948 expressing PMN-MDSC-derived TGF- β 1 promotes the epithelial-mesenchymal transition of
949 metastatic lung adenocarcinoma. *International Journal of Clinical and Experimental Pathology*,
950 13(6), 1361–1371.
- 951 47. Meyers, R. M., Bryan, J. G., McFarland, J. M., Weir, B. A., Sizemore, A. E., Xu, H., ... &
952 Tsherniak, A. (2017). Computational correction of copy number effect improves specificity of
953 CRISPR-Cas9 essentiality screens in cancer cells. *Nature genetics*, 49(12), 1779-1784.
- 954 48. Migita, T., Narita, T., Nomura, K., Miyagi, E., Inazuka, F., Matsuura, M., ... & Ishikawa, Y. (2008).
955 ATP citrate lyase: Activation and therapeutic implications in non-small cell lung cancer. *Cancer*
956 *research*, 68(20), 8547-8554.